Rapport de la réunion de printemps de la SSP

Autor(en): **[s.n.]**

Objekttyp: **AssociationNews**

Zeitschrift: **Helvetica Physica Acta**

Band (Jahr): **66 (1993)**

Heft 4

PDF erstellt am: **12.07.2024**

Nutzungsbedingungen

Die ETH-Bibliothek ist Anbieterin der digitalisierten Zeitschriften. Sie besitzt keine Urheberrechte an den Inhalten der Zeitschriften. Die Rechte liegen in der Regel bei den Herausgebern.
Die auf der Plattform e-periodica veröffentlichten Dokumente stehen für nicht-kommerzielle Zwecke in Lehre und Forschung sowie für die private Nutzung frei zur Verfügung. Einzelne Dateien oder Ausdrucke aus diesem Angebot können zusammen mit diesen Nutzungsbedingungen und den korrekten Herkunftsbezeichnungen weitergegeben werden.
Das Veröffentlichen von Bildern in Print- und Online-Publikationen ist nur mit vorheriger Genehmigung der Rechteinhaber erlaubt. Die systematische Speicherung von Teilen des elektronischen Angebots auf anderen Servern bedarf ebenfalls des schriftlichen Einverständnisses der Rechteinhaber.

Haftungsausschluss

Alle Angaben erfolgen ohne Gewähr für Vollständigkeit oder Richtigkeit. Es wird keine Haftung übernommen für Schäden durch die Verwendung von Informationen aus diesem Online-Angebot oder durch das Fehlen von Informationen. Dies gilt auch für Inhalte Dritter, die über dieses Angebot zugänglich sind.

Ein Dienst der *ETH-Bibliothek*
ETH Zürich, Rämistrasse 101, 8092 Zürich, Schweiz, www.library.ethz.ch

http://www.e-periodica.ch

Helv Phys Acta
Vol. 66 (1993)

0018-0238/93/040405-48$1.50+0.20/0

PROPAGATION DE PHASES NORMALES DANS LES SUPRACONDUCTEURS

N. Amaioua, E. Holguin et L. Rinderer

IPE de l'Université de Lausanne, 1015 Lausanne, Switzerland

Résumé: Nous présentons une théorie décrivant la propagation de plusieurs phases normales dans des supraconducteurs de type-I dont la résistivité est une fonction de l'espace. Les calculs montrent que ces phases n'interagissent pas si elles sont suffisamment éloignées, bien que leurs vitesses de propagation puissent subir de brusques modifications suite au changement de propriétés dans le milieu. Le modèle est en bon accord avec les résultats expérimentaux.

1. INTRODUCTION

Les expériences [1,2] montrent que la supraconductivité dans des fils peut être détruite par des courants I inférieurs à la valeur de Silsbee. Ce phénomène est notamment observé dans des échantillons impurs où les effets thermiques jouent un rôle important. Dans ce cas, une instabilité thermique crée d'abord une région normale qui s'étend ensuite le long du supraconducteur.

Nous étudions ici une situation plus complexe résultante d'une répartition non uniforme des impuretés; c'est-à-dire, lorsque la résistivité de l'échantillon à l'état normal varie en fonction de la position. Il s'établit alors une dissipation thermique différentielle qui peut provoquer la propagation de plusieurs zones normales ou l'arrêt de certaines d'entre elles.

2. MODELE THEORIQUE

Afin de simplifier le problème, considérons le cas d'un échantillon cylindrique de rayon r comportant une petite zone centrale de resistivité normale ρ_n', et qui est entourée par deux autres de longueur semi-infinie possédant la même résistivité $\rho_n \gg \rho_n'$. Supposons à présent que l'échantillon est initialement supraconducteur et, qu'un certain temps après, des instabilités thermiques créent deux zones normales Ng et Nd se propageant en direction de la zone centrale supraconductrice S' (Fig. 1a). Pour de faibles vitesses et lorsque la situation stationnaire est atteinte, l'équation régissant la température T dans une zone normale prend la forme

$$K \frac{d^2T}{dx^2} - \frac{2h}{r}(T-T_b) - q = o. \qquad (1)$$

$$\lim_{x \to x_1(t)} T(x,t) = \lim_{x \to x_2(t)} T(x,t) = T_t$$

où $K=K_N$, h, T_b, T_t et q sont respectivement la conductivité thermique, le coefficient de transfert de chaleur, la température du bain d'hélium, la température de transition et la chaleur de Joule dissipée par unité de volume ($K=K_s$ et q=o dans une zone S). D'autre part, la vitesse v de propagation peut se calculer en exprimant la conservation du flux de chaleur à travers l'interface N-S

$$- K_N \left(\frac{dT}{dx}\right)_{N-S} + K_S \left(\frac{dT}{dx}\right)_{N-S} = Lv \qquad (2)$$

Fig. 1a Progression de deux phases normales en direction de la zone centrale supraconductrice S'. A droite, on montre également la variation temporelle du voltage lorsqu'une de ces phases (Ng) pénètre dans la région des sondes de potentiel U.

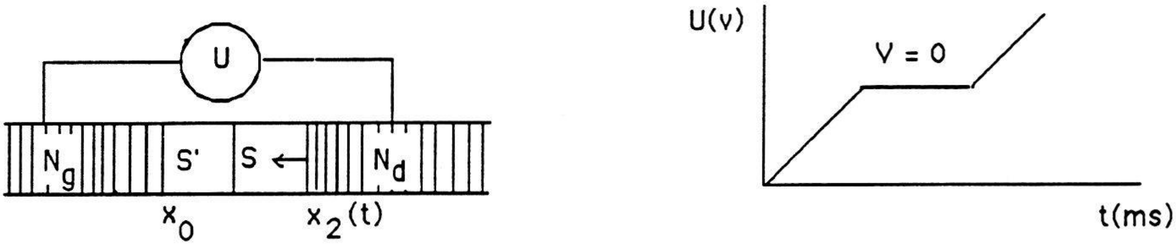

Fig. 1b La phase normale Ng est brusquement arrêtée aux bornes de la zone centrale supraconductrice S', alors que l'autre phase normale Nd continue sa progression. Le voltage, à droite, reste constant pendant un certain intervalle de temps, pour ensuite varier dès que la phase Nd pénètre dans la région des sondes de potentiel U.

où L est la chaleur latente. Au moyen des eqs. (1) - (2), on peut montrer que si

$$\rho_n' < \rho_{min} = \frac{4\pi^2 r^4 h(T_t - T_b)}{I^2} \qquad (3)$$

alors la dissipation par effet Joule n'est pas suffisante pour maintenir la progression de ces zones normales. Par conséquent, elles s'arrêteront l'une après l'autre aux bornes de la zone centrale (Fig. 1b). Le voltage présentera alors deux segments de droite avec une pente non nulle reliés par un palier horizontal, ainsi que Casas [3] l'a observé dans des expériences réalisées sur des échantillons d'étain.

3. CONCLUSIONS

Notre modèle traitant la propagation de plusieurs phases normales généralise le problème de la destruction thermique de la supraconductivité. Il permet de comprendre de nombreux résultats expérimentaux ne trouvant pas une explication satisfaisante à l'intérieur du cadre de la propagation d'une seule phase normale.

Ce travail a été réalisé grâce à l'appui financier du Fonds National Suisse pour la Recherche Scientifique.

REFERENCES:

1. W.C. Overton, J. Low Temp. Phys. **5**, 397 (1971).
2. E. Posada and L. Rinderer, J. Low Temp. Phys. **21**, 223 (1975).
3. J. Casas and L. Rinderer, J. Low Temp. Phys. **76**, 17 (1989).

Current induced resistive states in superconducting films

A. Cossy-Favre†, B. Dutoit*, E. Holguin, I. Landau[a] and L. Rinderer

Institut de Physique Expérimentale, Université de Lausanne, 1015 Lausanne, Switzerland

[a]On leave from Kapitza Institute for Physical Problems, 117334 Moscow, Russia

We present an experimental study of the current induced destruction of superconductivity in thick cylindrical indium films. The most interesting aspect of these experiments is the possibility to observe and investigate different mechanisms of the superconductivity destruction depending on the ratio of the sample thickness d to the coherence length $\xi(T)$. If $d/\xi(T)<4.5$ we observed a resistive state throughout the section of the film, but in the case of $d/\xi(T)>4.5$ the destruction of superconductivity started with the formation of a normal shell along the outer surface of the sample together with a thin layer of the two-dimensional mixed state at the inner surface.

The destruction of superconductivity by a current in hollow cylindrical samples of type-1 superconductors is of particular interest due to appearing a thin layer of so called two-dimensional mixed state (TM-state), which is not an intermediate one, i.e. does not represent a mixture of macroscopic domains of superconducting and normal phases. The existence of this special resistive state was postulated by L.D. Landau in 1938 [1] and it was discovered experimentally only 30 years after [2]. A considerable number of papers on this subject were published so far, but, nevertheless, even the qualitative picture of the TM-state remains unclear, not to say about a consistent theory. Earlier the TM-state of type-1 superconductors has been studied only in bulk samples. This state should exist also in cylindrical films if the wall thickness d is large enough (d has to be larger, at least, than the TM-state thickness). The TM-state thickness δ must be of the order of the coherence length $\xi(T)$ and the best way to investigate different situations depending on the ratio $d/\xi(T)$ is to provide measurements at different temperatures near T_c.

In the case of the current induced resistive state studying it is convenient to use two critical currents: the first I_{c1} for the transition from superconducting to the resistive state and the second I_{c2} for the resistive-normal state transition. We have measured these two critical currents as well as critical magnetic fields of our samples.

Critical magnetic fields measurements in films make it possible to find the magnetic field penetration depth $\lambda(T)$, coherence length $\xi(T)$ and the critical magnetic field for the bulk H_{c0} (here we keep in mind a bulk sample of the same material as in the film, so, H_{c0} values for different films should be slightly different). Determination of H_{c0} allows to compare experimental critical currents with Silsbee's critical value

---

† Present address: Institut für Physik, Universität Basel, 4056 Basel, Switzerland.
* Present address: Federal Institute of Technology, 1015 Lausanne, Switzerland.

$$I_{c0} = \frac{cr_0 H_{c0}}{2}$$

Experiments were provided on indium films evaporated on quartz rods. Diameters of our rods were about 0.3 mm. We have investigated few films of different thickness between 0.3 μ and 6 μ.

We observed a large difference in a CVC behaviour depending on the $d/\xi(T)$ ratio and fig. 1 shows corresponding dependences of the sample resistance.

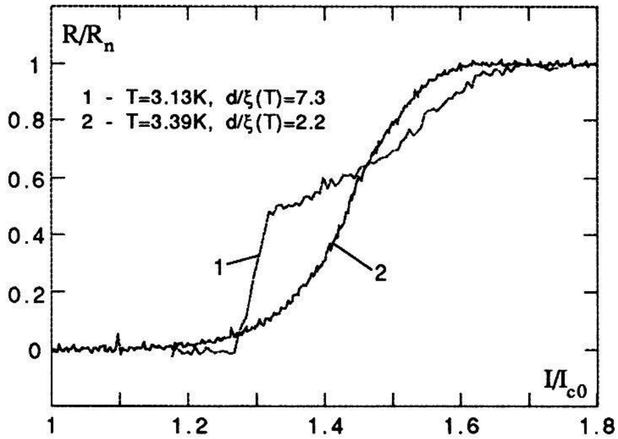

Fig. 1. Dependences of the sample resistance on the current for the sample with d=5.5 μm and T_c=3.416K.

At low temperatures we had a resistance jump at $I=I_{c1}$ and a large current region of the resistive state. This initial increase of the resistance corresponds to the creation of the normal shell and of the TM-state layer inside the sample.

At high temperatures we had smooth CVC. This region corresponds to comparatively large $\xi(T)$ and the sample thickness was not sufficient for the TM-state existence. The type of the resistive state in this case should be similar to that in very thin films ($d \ll \lambda(T)$).

Transition from one type of CVC to another was sharp enough and allowed to find the boundary temperature $T \approx 3.3$K and the corresponding minimal thickness of the sample necessary for the formation of the TM-state $d_{min} \approx 4.5\xi(T)$.

Measurements of the resistance jumps at the low temperature region made it possible to calculate the TM-state thickness $\delta \approx 3.8\xi(T)$. We want to emphasize that it is the first measurement of the TM-state thickness and this result is in a good agreement with the simple picture based on the Ginzburg-Landau theory.

Among other results the most astonishing is that the ratio I_{c1}/I_{c0} practically does not depend on the temperature for all the samples in spite of very large variations $d/\lambda(T)$ and $d/\xi(T)$ over this temperature range. Another interesting result is that for the thick-wall sample (d=5.5 μ) I_{c1} sufficiently larger I_{c0}; as we know, this is the first experimental observation of a superconducting state in type-1 superconductors existing in the situation, when the magnetic field of the current considerably exceeds H_{c0}.

References

1. L. D. Landau, private communication to D. Shoenberg; see D. Shoenberg Superconductivity. University Press, Cambridge (1938), p. 59.

2. I. L. Landau and Yu. V. Sharvin, Sov. Phys. JETP Lett. 10 (1969), 121.

The effect of Fermi Surface geometry on the superconductivity given by spin fluctuations in $La_{2-x}Sr_xCuO_4$

B. Barbiellini, J. Magnin and M. Peter

DPMC, Université de Genève, CH-1211 Genève 4, Switzerland.

Superconductivity due to the spin fluctuation mechanism of Moriya *et al* [1] and Monthoux *et al* [2] is treated for a realistic Fermi Surface (FS) of $La_{2-x}Sr_xCuO_4$, obtained from self-consistent LMTO band structure calculations. For the coupling, a strongly peaked susceptibility around the Brillouin zone corner is used. We find that the Fermi surface shape can influence significantly the T_c and that the most favorable case is obtained by doping with divalent Sr around $x = 0.15$.

We have performed a selfconsistent LMTO band calculation using Local Density Approximation (LDA) on the body-centered tetragonal phase of La_2CuO_4 [3]. Near the Fermi energy the Cu $d(x^2 - y^2)$ and O $p(x,y)$ bands have strong antibonding character. The nearest-neighbor tight-binding model, which is too crude for our purposes, leads to the square FS $|k_x a| + |k_y a| = \pi$ with the corners $\pm(\pi/a, 0)$, $\pm(0, \pi/a)$, at the half-filled limit ($x = 0$), whereas the selfconsistent LDA calculation gives a holelike FS (figure 1). In the following, we will neglect the small z dispersion of the FS and we will treat the Sr doping in a rigid band model. The points $\pm(\pi/a, 0)$, $\pm(0, \pi/a)$ are on the FS for a certain concentration of doping around $x = 0.15$ (figure 2).

We suppose that the pairing interaction occurs only in a narrow layer near the FS, with a thickness $2\omega_c$. We divide the FS into N parts and the gap equation at $T = T_c$ reduces to a $N \times N$ secular equation [4] given by $\det(\mathbf{1}\lambda - \mathbf{g}) = 0$, where $\mathbf{g}$ is the coupling matrix and λ is the largest eigenvalue. Then $T_c = 1.14\omega_c \exp(-1/\lambda)$. In the present calculations, we use $N \sim 100$.

The susceptibility χ given by Moriya *et al* as $\chi(\vec{q}) = \frac{1}{2IA\kappa^2} \sum_{\vec{Q}} \exp -(\frac{\vec{q}-\vec{Q}}{\kappa})^2$, is strongly peaked around the Brillouin zone corner when $Q = (\pm\pi/a, \pm\pi/a)$. I is the intra-atomic exchange constant, κ is the inverse antiferromagnetic correlation length and A is a parameter having the dimension of a surface. In contrast to the conventional one phonon pair attraction, the one spin fluctuation exchange process leads to a repulsion between opposite spin particles. For a repulsive coupling the pairing can occur only if the order parameter changes sign around the FS (for instance the gap could be a d-wave [1, 2]) or if it oscillates with energy [5]. The coupling matrix for the even parity paring (opposite spin particles) is given by $g(\vec{k}, \vec{k}') = C_0 + \frac{C}{\kappa^2} \sum_{\vec{Q}} (\exp -(\frac{\vec{k}-\vec{k}'-\vec{Q}}{\kappa})^2 + \exp -(\frac{\vec{k}+\vec{k}'-\vec{Q}}{\kappa})^2)$, where the constant C_0 does not belong to a channel giving superconductivity and therefore it can be decoupled from the gap equation. Thus the present coupling depends only on the inverse antiferromagnetic correlation length κ and the constant $C = \frac{3}{4}\frac{N(E_F)}{N} I/A$. The eigenvalue λ scales with C/κ^2. The parameters we use are the typical ones: $I = 0.1$ eV, $\kappa = 0.354/a$ and $A = 0.1a^2$. The numerical results are the following: λ is respectively $0.366N(E_F)$, $0.496N(E_F)$, $0.608N(E_F)$, $0.365N(E_F)$, when x is 0, 0.10, 0.15 and 0.19. If the FS is the perfect square with the corners $\pm(\pi/a,0)$, $\pm(0,\pi/a)$, we obtain the optimal value $\lambda = 0.662N(E_F)$. The case $x = 0.15$ and $N(E_F) = 1.73$ eV^{-1} gives $T_c = 35$, if $\omega_c = \omega_{SF}/(\kappa a)^2$, where $\omega_{SF} = 10$ K is the paramagnon energy. However according to Monthoux and Pines [6], a realistic estimation of T_c should be done in strong coupling and must take full account of the momentum and the frequency dependence.

From our calculations on the $La_{2-x}Sr_xCuO_4$, one may deduce that the main effect of doping is to produce the optimal FS shape. However this is not always the case. For the electron doped superconductors $Nd_{2-x}Ce_xCuO_4$, we find rounded Fermi surfaces around $Q = (\pm\pi/a, \pm\pi/a)$ [3], which do not have the corners $\pm(\pi/a,0)$, $\pm(0,\pi/a)$, and therefore small effects on the T_c: λ is respectively $0.33N(E_F)$, $0.35N(E_F)$, $0.36N(E_F)$ when x is 0, 0.15 and 0.22.

In figure 3 the gap function for the FS $|k_x a| + |k_y a| = \pi$ is shown along the line $(\pi/a,0)$-$(0,\pi/a)$, its symmetry is of the $d(x^2-y^2)$ type. The case obtained by doping with Sr around $x = 0.15$ gives a similar picture. An interesting feature is that the gap function remains small for a wide range on the FS. This is due to the sharp peak of the susceptibility [1].

For the odd parity pairing (parallel spin particles), $g(\vec{k},\vec{k}') = \frac{C}{\kappa^2}\sum_{\vec{Q}}(\exp -(\frac{\vec{k}-\vec{k}'-\vec{Q}}{\kappa})^2 - \exp -(\frac{\vec{k}+\vec{k}'-\vec{Q}}{\kappa})^2)$, $C = -\frac{1}{4}\frac{N(E_F)}{N}I/A$ and $\lambda_{odd} < \lambda_{even}$. In particular $\lambda_{odd} = 0.132N(E_F)$ for the FS $|k_x a| + |k_y a| = \pi$. In this case, the eigenfunction symmetry is of the p type.

We are grateful to Dr. T. Jarlborg, P. Lerch and Prof. M. Weger for stimulating discussions. One of us (M.P.) wishes to thank Prof. T. Moriya for the hospitality during his visit in Japan at the ISSP.

References

[1] T. Moriya *et al*, J. Phys. Soc. Jpn. **59** (1990) 2905
[2] P. Monthoux *et al*, Phys. Rev. B **46** (1992) 14803
[3] P. Blandin *et al*, Phys. Rev. B **46** (1992) 390
[4] M. Peter *et al*, Helv. Phys. Acta **50** (1977) 267
[5] M. Weger, Physica B **172** (1991) 261
[6] P. Monthoux and D. Pines, Phys. Rev. Lett. **69** (1992) 961

Figure 1

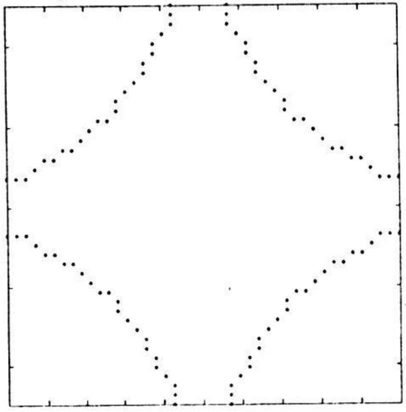

Figure 2

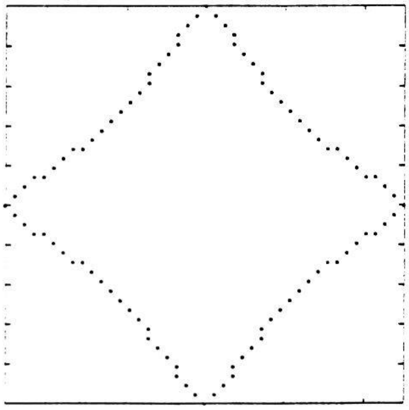

Figure 3

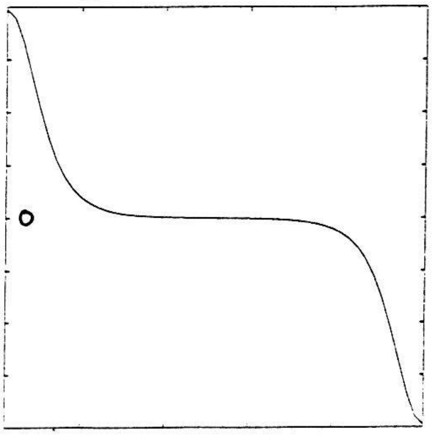

The Fractal Dimension of Xenon Dendrites

U. Bisang and J.H. Bilgram
Laboratorium für Festkörperphysik, ETH, CH 8093 Zürich

Dendritic structures can be characterized by parameters, which describe the integral dendrite. The fractal dimension is an example of such an integral parameter. We have determined the fractal dimension d_f of the contour of the projection of a dendrite at various supercoolings over a range of more than two orders of magnitude in length scale. d_f does not depend on supercooling. $d_f = 1.42 \pm 0.05$.

We study xenon dendrites during growth into a three-dimensional volume of supercooled, pure melt [1]. Parameters that characterize individual sidebranches do not lead to reproducible results. This behaviour is characteristic for dynamical chaotic systems. We have found that integral parameters, which describe properties of the integral dendrite, are suitable to characterize dendrites, because these parameters take account of the nonlinear interactions between the different sidebranches [1]. Integral parameters are, e.g. the volume or the surface of a dendrite. Another integral parameter is the fractal dimension. We have determined the fractal dimension d_f of the contours of two-dimensional projections of xenon dendrites at various supercoolings. Calculations of the fractal dimension have been performed in two different ways. First with the "box counting method", which can be easily derived from the definition of the fractal dimension $d_f = \lim_{\varepsilon \to 0} \ln N(\varepsilon)/\ln(1/\varepsilon)$. $N(\varepsilon)$ is the number of "boxes" needed to cover the entire fractal set. ε is a typical length of these boxes. For small ε the number of "boxes" $N(\varepsilon)$ must have an asymptotic behaviour of the form $\log N(\varepsilon) \sim -d_f \log \varepsilon$.

Video pictures of the contour are covered with "boxes" of size ε and $N(\varepsilon)$ is determined for various ε. Fig. 1 shows $\log N(\varepsilon)$ vs. $\log \varepsilon$ for a xenon dendrite. We find that the contour is fractal over a range of about two orders of magnitude in length scale and about three orders in the number of "boxes", neglecting the data points for the smallest "box sizes". The fractal dimension d_f is called box dimension. The range of the length ε is limited for large values by the limited size of our picture. Small length scales are limited by the size of the pixels of our video system. The deviation from the power law at small length scales in Fig. 1 is due to the limited size of the pixels. To verify our results we used a correlation method developed by Grassberger [2]. $\log C(r) \sim \nu \log r$. $C(r)$ is a correlation function, r a length and ν is the so called correlation dimension with $\nu \leq d_f$. In Fig. 2 $\log C(r)$ is plotted vs. $\log r$. For small r a slope 1 is expected. Again we assume that the pixel size is limiting our evaluation at small length scales.

The fact that both methods lead, within the precision of the data, to the same results, indicates that the contour is indeed fractal over a range of about two orders in length scale.

Using both methods, we have calculated the fractal dimensions ν and d_f at different times during the growth of a xenon dendrite. We find that after a short transient time, the fractal dimensions do not depend on the age of the dendrite. To minimize the statistical errors we have calculated the averaged fractal dimensions $\bar{d}_f$ and $\bar{\nu}$ of several ages of a specific dendrite. Fig. 3 shows $\bar{d}_f$ and $\bar{\nu}$ calculated for various supercoolings. The fractal dimensions do not depend on supercooling.

Both methods lead within the precision of the data to the same results, although the correlation method seems to lead to systematically slightly higher values for $\bar{\nu}$. This might be the effect of a systematic error in the algorithm.

The averaged fractal dimension is $\bar{d}_f = 1.42 \pm 0.05$ (box dimension).

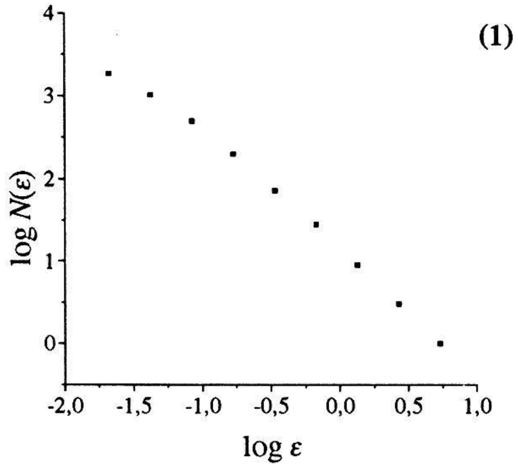

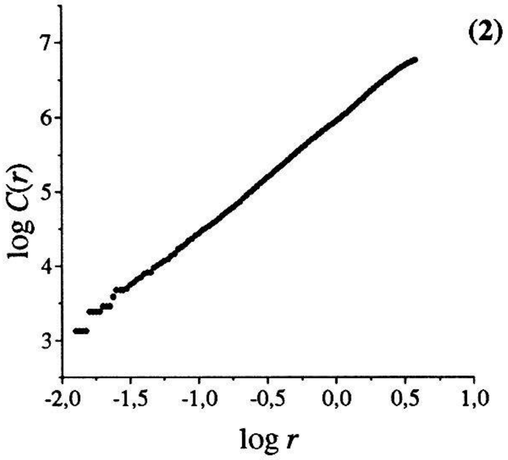

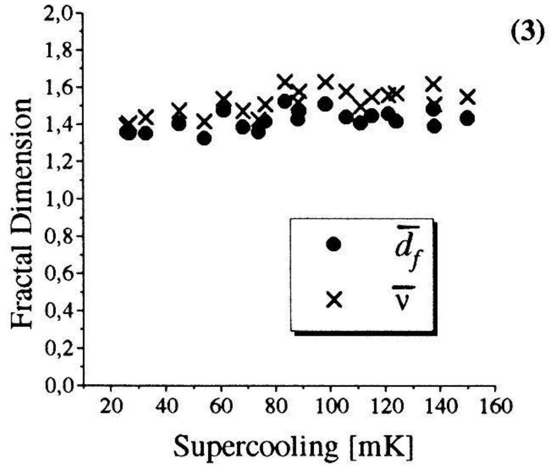

Fig. 1 Number of "boxes" $N(\varepsilon)$ vs. the length scale ε of the "boxes". From the scaling we estimate a fractal dimension $d_f \approx 1.4$.

Fig. 2 Correlation function $C(r)$ vs. the length scale r. From the scaling we can estimate the correlation dimension ν.

Fig. 3 Averaged box dimension $\bar{d}_f$ and the averaged correlation dimension $\bar{\nu}$ vs. the supercooling of the melt.

Acknowledgements: We thank Prof. H.R. Ott for his support. This work is supported by Swiss National Science Foundation.

[1] E. Hürlimann, R. Trittibach, U. Bisang, and J.H. Bilgram Phys. Rev. A **46**, 6579 (1992).
[2] P. Grassberger and I. Procaccia, Phys. Rev. Lett. **50**, 346 (1983).

Atomic Force Microscopy Used for the Characterization of Precipitated Colloidal Particles

U. D. Schwarz, J. Bohonek[a], H. Haefke, W. Sager[b],
R. Steiger[a] and H.-J. Güntherodt
Institute of Physics, University of Basel, Switzerland; [a] Ilford AG, Fribourg, Switzerland;
[b] School of Chemistry, University of Hull, United Kingdom

Colloidal particles play an important role in advanced materials science since their size, shape and structure can be controlled and influenced in a wide range. These parameters can be determined by atomic force microscopy.
In this work, photographic AgBr microcrystals as well as amorphous nanoceramics consisting of TiO_2, $FeYO_3$ or Fe_2O_3 particles were studied and characterized on different imaging scales. Surface fine structures on the silver halide microcrystals as well as the amorphous-crystalline transition of the oxide particles will be discussed.

Modern materials science is aimed at controlling all parameters connected with material properties on the nanometer or even on the atomic scale. These requirements are met for colloidal particles grown in emulsion droplets which act as micro-reactors. The growth conditions can be influenced down to the atomic level what enables the preparation of small particles with well-defined sizes, shapes and structures even while producing industrial quantities. Atomic force microscopy (AFM) is not only able to determine accurately these parameters, but also further material properties can be investigated. We applied AFM to two different colloidal particle systems.

Photographic AgBr microcrystals are, in spite of their relative large dimensions (0.4-5 μm), only difficult to examine with conventional optical or electron-optical methods since they are highly beam-sensitive. AFM, profiling surfaces with a sharp tip, is therefore ideally suited for the characterization of such samples, as yet reported [1]-[4]. Imaging of AgBr microcrystal ensembles of cubic, octahedral and tabular shapes reveals morphological details like growth hills (Fig. 1a) or surface steps (Fig. 1b) arising from gliding of twin planes. Furthermore, topological changes due to photolysis can be studied (cf. Fig. 1c).

Nanometer-sized oxide particles have recently attracted interest in ceramic processing research since they allow the design of ceramic components with new properties for high-technology applications. To prepare such particles, a new precipitation route has been developed and applied to produce Fe_2O_3, TiO_2 and $FeYO_3$ particles [5]. AFM exhibited particle diameters of 10-40 nm and smooth surfaces on the precursor particles. Thin layers of precursor particles were deposited on a substrate and the transition from the amorphous to the crystalline state was investigated. AFM revealed significant changes in layer morphology and particle sizes dependent on the annealing temperature (Fig. 2).

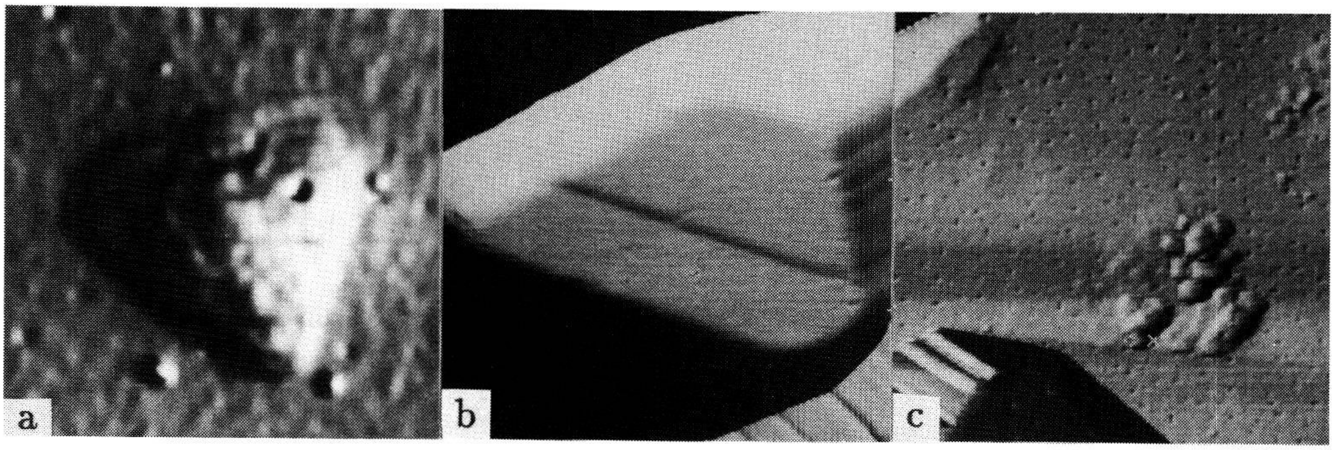

Fig. 1: (a): Growth hill on a {111} top surface of a tabular AgBr microcrystal. The three sides of the basal plane are parallel to the ⟨110⟩ directions of the AgBr lattice and 600 nm long. The height of the hill is determined to be 14 nm. (b): 20 nm high surface step (parallel to one side of the tabular microcrystal) which arises from dislocation gliding through the twin plains [6] (image size: 1.6 μm × 1.6 μm). (c): Tabular microcrystal exposed to light. The formation of small hills in triangular arrangement, consisting of print-out silver, and of small holes can be observed (image size: 3 μm × 3 μm).

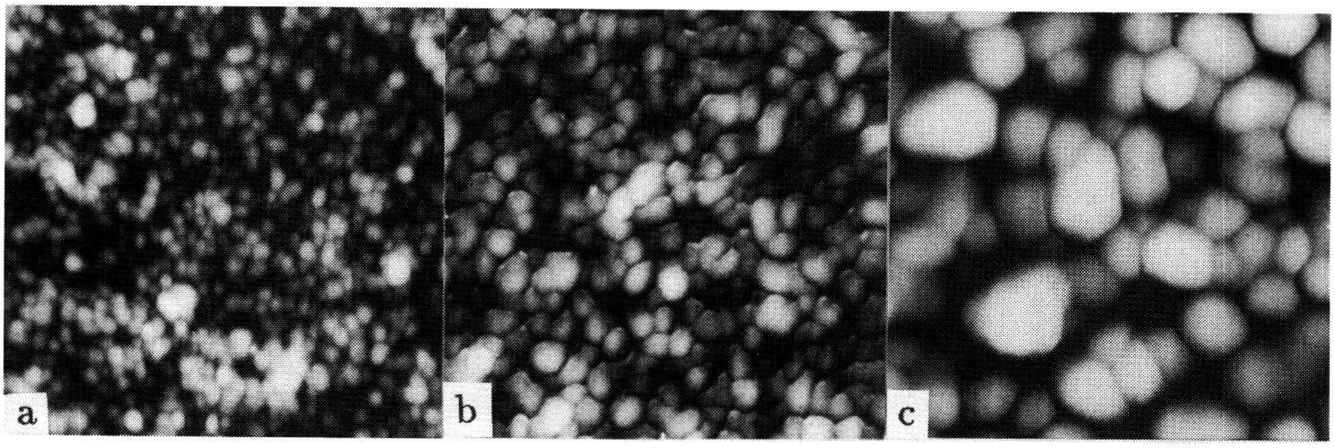

Fig. 2: AFM micrograph (500 nm × 500 nm) of a thin layer of colloidal Fe_2O_3 particles after annealing for 1/2 h at 500 °C (a), 600 °C (b) and 1000 °C (c). Up to 500 °C, the particle size does not change (always ~10-40 nm); significant growth starts at 600 °C (particle sizes 17-53 nm). At 1000 °C, particle sizes ranging from 40 nm to 130 nm are observed. The amorphous-crystalline transition temperature was determined to be between 500 °C and 600 °C by x-ray diffraction.

References

[1] U. D. Schwarz et al., Ultramicroscopy **41**, 435 (1992).
[2] U. D. Schwarz et al., J. Imaging Sci. Technol. **36**, 361 (1992).
[3] U. D. Schwarz et al., Helv. Phys. Acta **65**, 874 (1992).
[4] U. D. Schwarz et al., submitted to J. Imaging Sci. Technol.
[5] W. Sager et al., Colloids and Surfaces, in press.
[6] J. F. Hamilton, Photogr. Sci. Eng. **11**, 57 (1967).

Investigation on ferroelectric domains and domain walls with scanning force microscopy

R. Lüthi, H. Haefke, K.-P. Meyer†, E. Meyer, L. Howald, M. Rüetschi,
R. M. Overney and H.-J. Güntherodt

Institute of Physics, University of Basel, Klingelbergstr. 82, CH-4056 Basel, Switzerland;
†MPI of Microstructure Physics, D-O-4050 Halle (Saale), Germany.

We used a scanning force microscope (SFM) to study the domain structures of ferroelectric GASH crystals. The SFM was operated in the static contact as well as dynamic non-contact mode. In the static contact mode the ferroelectric plus and minus domains show opposite contrast. Operating the SFM in the dynamic non-contact mode the domain walls are revealed. The latter technique was improved and its advantage in comparison with scanning electron microscopy is discussed.

Ferroelectric domains and domain walls on ferroelectric crystals of GASH (guanidinium aluminum sulfate hexahydrate; $C(NH_2)_3Al(SO_4)_2 \cdot 6H_2O$) were studied with scanning force microscopy (SFM). GASH belongs to the trigonal crystal system; the space group is $P31m$ with a=1.1738 nm and c=0.8951 nm [1]. The spontaneous polarization is parallel to the crystallographic c axis and was determined to be 0.35 $\mu C/cm^2$ at room temperature. The GASH(0001) surfaces were prepared by cleaving the crystals perpendicular to the polar axis. The cleavage structure of GASH crystals studied with SFM was reported elsewhere [2].

The force microscopes used were operated in the static contact mode (repulsive force regime) and in the dynamic non-contact mode (attractive force regime) [3]. Images of constant force and maps of constant gradient relief are obtained with these operating modes. Using the non-contact method, an actual lateral and vertical resolution of 1 nm and 0.1 nm, respectively, could be achieved [4].

Figure 1 shows a SFM image of a GASH(0001) cleavage face revealing the typical elementary cleavage structure. Superimposed to this surface structure the image exhibits ferroelectric domains of various shapes. Plus and minus domains show opposite contrast. The image contrast could be improved by scanning perpendicular to the length axis of the cantilever, i.e. at a scan angle of about 90°. Furthermore, the contrast of the domains is changed by recording the forward and backward scan, respectively. Lateral forces together with the possibility of the Si_3N_4 tip to trap charge easily play an important role in the imaging process. Whereas in the contact mode plus and minus domains are visualized, in the non-contact mode the image reveals domain walls (cf. fig. 2). Up to now, smallest full width at half maximum of about 50 nm at a domain wall was measured. The force gradient was on the order of 10^{-3} N/m. To clarify the nature of the domains, the same cleavage face was inspected with a scanning electron microscope (see fig. 3) which has found to be sensitive to ferroelectric domain walls at specific operation conditions [5]. An extended discussion is in preparation [6].

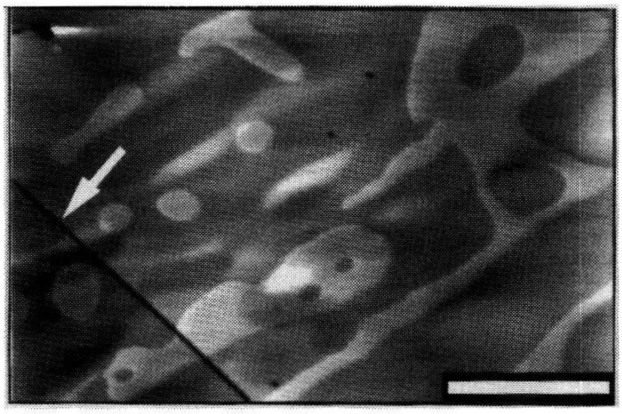

Figure 1:
Force micrograph of a GASH surface operating the SFM in the repulsive contact mode. The cleavage step (marked by arrow) was determined to be 0.9 nm in height, which corresponds to one unit cell spacing along the c axis. Superimposed to this cleavage structure the image exhibits ferroelectric domains of various shapes and opposite contrast. The scale bar corresponds to 10 μm.

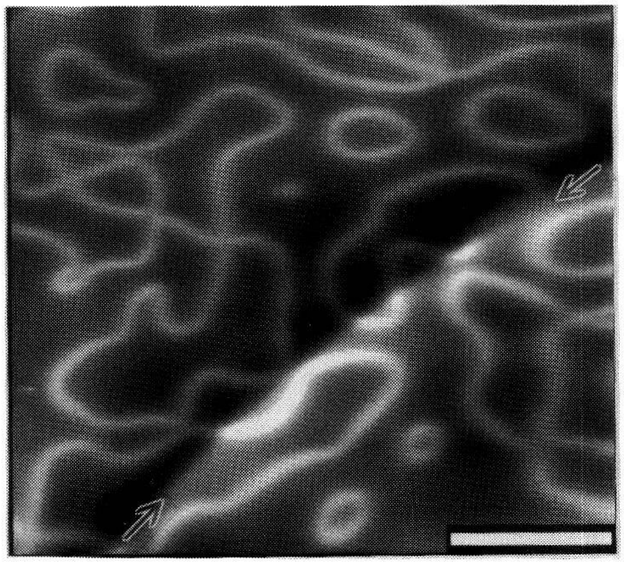

Figure 2:
Force gradient micrograph of a GASH surface operating the SFM in the dynamic non-contact mode. Overlaying to a huge cleavage step the image reveals ferroelectric domain walls (bright lines). The cleavage steps (marked by arrows) run through the domains without significant bending. We could not observe an influence of the cleavage structure due to the domain walls. The scale bar corresponds to 10 μm.

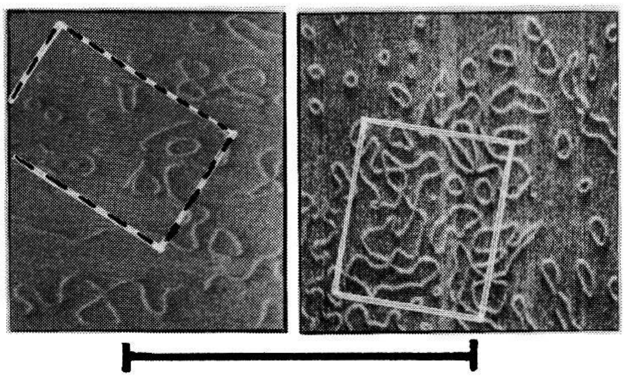

Figure 3:
Scanning electron micrographs of the GASH cleavage face studied. The SEM was equipped with a field emission electron source and was operated at an acceleration voltage of 1 kV in the second electron emission mode. The ferroelectric domain walls can be identified by the bright lines. The areas imaged with SFM are indicated by dashed (cf. fig. 1) and solid (cf. fig. 2) squares. The scale bar corresponds to 60 μm.

References

[1] B.J.B. Schein, E.C. Lingafelter and J.M. Stewart, *J. Chem. Phys.* **47**, 5183 (1967).

[2] R. Lüthi, H. Haefke, P. Grütter, H.-J. Güntherodt, L. Szcześniak and K.-P. Meyer, *Surf. Sci. Lett.* **285**, L498 (1993).

[3] For a recent review: E. Meyer, *Progr. Surf. Sci.* **41**, 3 (1992).

[4] D. Anselmetti, R. Lüthi, E. Meyer, T. Richmond, M. Dreier, J. Frommer and H.-J. Güntherodt, *submitted to Science.*

[5] R. Le Bihan and G. Jouet, *Ferroelectrics* **26**, 843 (1980).

[6] R. Lüthi, H. Haefke, H.-J. Güntherodt and K.-P. Meyer, *in preparation.*

Probing Low-Energy Scales with High-Energy Spectroscopies in Heavy-Fermion Materials

M. Grioni, D. Malterre, P. Weibel, B. Dardel and Y. Baer
Institut de Physique, Université de Neuchâtel, CH-2000 Neuchâtel, Switzerland

Abstract. We have investigated with high-resolution photoelectron spectroscopy some fundamental predictions of the Anderson impurity model. The experimental *4f* signal exhibits characteristic changes with temperature in $YbAgCu_4$, and with hybridization in $CeSi_x$. These results lend strong experimental support to the interpretation of the spectral properties of heavy fermions based on the Anderson model.

The fundamental rôle that electron spectroscopies have played in the investigation of strongly correlated materials reflects the close connection between the spectral function, as measured in a combined photoemission (PES) and inverse photoemission (BIS) experiment, and the one-particle Green's function of the interacting system. The accepted scenario for Ce- and Yb-based mixed-valent or heavy fermion materials is based on the Impurity Anderson Model (IAM). The IAM spectral function exhibits structures at all the relevant energy scales of the problem: charge fluctuations ($U \sim 5\text{-}10$ eV), spin-orbit (SO; $\Delta_{SO}=0.3$ eV), crystal field (CEF; $\Delta_{CEF}<0.1$ eV) and finally the Kondo scale k_BT_K, associated with the spin fluctuations that define the thermodynamic and transport properties (the model explicitely neglects coherence phenomena). A unique feature of the spectral function, revealing the many-body nature of the ground state, is the sharp Kondo resonance (KR), centered at k_BT_K above (below) E_F in cerium (ytterbium) materials. A crucial prediction of the IAM maintains that the KR exhibits approximate scaling behaviors defined by the strength of the hybridization between *4f* and delocalized electrons, and by the reduced temperature T/T_K. We have experimentally tested this prediction by investigating the temperature dependence of the PES and BIS spectra of selected Ce and Yb compounds, and the evolution of the PES spectral function in the paradigmatic system $CeSi_x$.

a) Temperature-dependence

The temperature dependence of the KR can be observed in BIS spectra of Ce materials and, due to electron-hole symmetry, in PES spectra of Yb compounds. We have discussed the Ce BIS results elsewhere [1]. Fig. 1 shows temperature-dependent high-resolution PES spectra of $YbAgCu_4$ ($T_K \sim 60K$). The spectra, normalized on temperature-independent band features at higher binding energy, reflect the intensity reduction of the KR and the CEF sideband (not resolved) with increasing temperature. Within the model this loss of spectral weight indicates the transition from a low-temperature local Fermi liquid to localised moments (for $T \gg T_K$). In the inset, the temperature-dependent integrated *4f* intensity, obtained after subtraction of the band contribution, is in remarkable agreement with the results of a calculation performed within the non crossing approximation (NCA) of the Anderson model.

b) The correlation between T_K and the spectral function in $CeSi_x$

$CeSi_x$ is a Kondo system where, by decreasing the Si concentration below x=2, the *4f*-band hybridization strength and therefore T_K are strongly reduced while the non-*f* DOS remains largely unaffected. T_K is close to 100K in $CeSi_2$, while a ferromagnetic order, with reduced moments, appears below 10K for x<1.8. Fig. 2 shows high-resolution PES spectra for selected x values. While the SO peak is rather insensitive to the Si concentration, the peak near E_F (the tail of the KR and the CEF sideband) is strongly depressed with decreasing x. The ratio of the two *4f* features (inset), obtained after subtraction of a constant non-*f* DOS, is shown to track with the Curie-Weiss temperature (Θ_{CW}, proportional to T_K) determined by magnetic measurements [2].

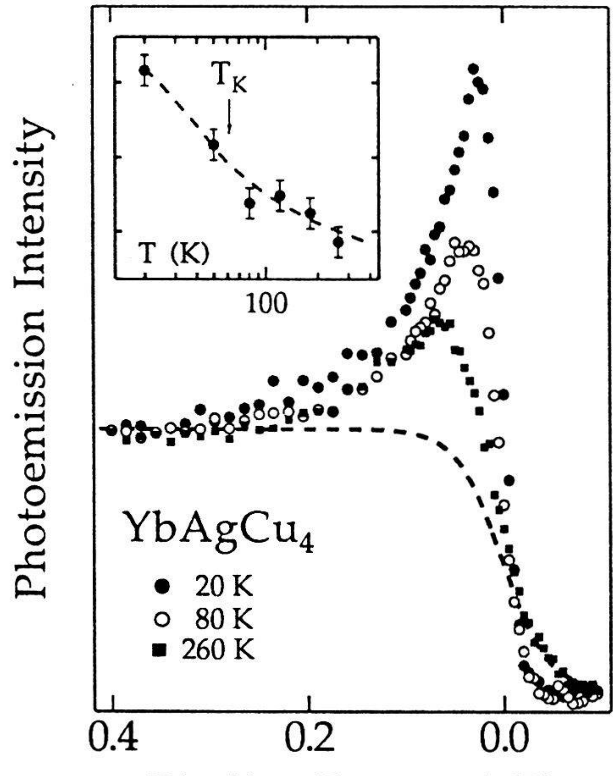

Fig.1. HeII PES spectra of $YbAgCu_4$. The dashed line represents the band emission. **inset**: the *4f* spectral weight (dots) is compared with an NCA calculation (dashed).

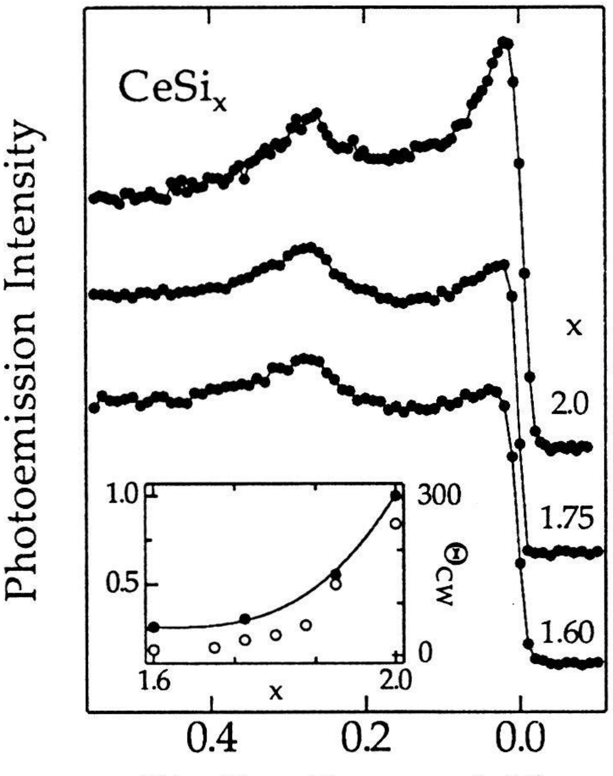

Fig.2. HeII PES spectra of $CeSi_x$. **Inset**: The ratio of the two *4f* peaks (full symbols, left scale) is compared with the Curie-Weiss temperature (empty symbols, right scale)

References:

1. Malterre D., Grioni M., Weibel P., Dardel B., Baer Y., Phys. Rev. Lett. **68**, 2656 (1992); and Europhys. Lett. **20**, 445 (1992).
2. S.A. Shaheen and J.S. Schilling, Phys. Rev. B**35**, 6880 (1987).

Non-Fermi liquid behaviour from photoemission spectroscopy of one-dimensional organic conductor $(TMTSF)_2PF_6$.

B. Dardel, D. Malterre, M. Grioni, P. Weibel and Y. Baer
Institut de physique, Université de Neuchâtel, CH-2000 Neuchâtel.

Abstract : High resolution photoemission experiments on the quasi-1D organic conductor $(TMTSF)_2PF_6$ in its normal phase show the absence of the Fermi edge singularity. This behaviour reflects the breakdown of the Fermi liquid picture and is due to the singular electronic correlations in 1D. Comparison with calculations of the spectral function in the framework of the Tomonaga-Luttinger model suggests that the correlation exponent α is very large ($\alpha>1$), corroborating the recent NMR measurements.

Recently it has been shown that One-Dimensional (1D) Charge-Density-Wave (CDW) materials (such as the blue bronze $K_{0.3}MoO_3$) do not exhibit the usual Fermi edge singularity characteristic of higher dimensional metals. This result has been discussed in terms of the singular behaviour of 1D systems and three possible causes for this lack of intensity at E_F have been proposed [1]:

1) Fluctuations associated with the CDW transition leading to the opening of a pseudogap in the metallic phase.
2) 1D singular correlations which yield a vanishing intensity of the spectral function at the Fermi energy.
3) Polarons which can induce a transfer of spectral weight to higher binding energies.

In order to discriminate between the different mechanisms, we present a photoemission study of a quasi-1D organic compound $(TMTSF)_2PF_6$. This metal is a good metallic conductor at high temperature and exhibits a phase transition at 12 K toward a Spin-Density-Wave insulating ground state. A large amount of experimental data shows that electronic correlations are the dominant interactions in this material [2], so that polaronic mechanisms and fluctuations can be neglected.

The photoemission spectra were taken with an Helium discharge lamp. The energy resolution was better than 20 meV. Samples were cleaved in ultra-high-vacuum. Figure 1 shows the HeII photoemission spectrum of $(TMTSF)_2PF_6$ at 50 K (metallic phase). It is dominated by broad structures with the shallowest one at -1.2 eV and a very weak spectral weight is found at the Fermi energy. A close up of the region near the Fermi level clearly shows that no Fermi edge is detectable, as previously observed in 1D inorganic compounds. The absence of photoemission weight near E_F clearly indicates that the usual Fermi liquid picture breaks down in these 1D materials.

Tomonaga and Luttinger [3] have proposed a simple, exactly solvable, model for interacting 1D electrons with a linearised dispersion. The salient features of the model are: a) the absence of quasi-particules, b) spin-charge separation and c) decay, with non-universal power laws, of all correlation functions. As an example, the integrated spectral function vanishes at the Fermi energy according to the asymptotic power law $\rho(\omega) \sim \omega^{\alpha}$, where α reflects the coupling strength which depends on the model parameters.

In figure 2 we report the calculated momentum integrated spectral function for several values of α at zero temperature. In the non-interacting limit ($\alpha=0$) the spectral density would be a constant. For $\alpha<1$ the spectral function exhibits an infinite slope at E_F, while the slope is 0 for $\alpha>1$. Comparison with the figure 1 shows that our data are consistent with $\alpha>1$. This large α value suggests that the long range interactions are important in this material since a maximum value of 1/8 is expected for the infinite-U Hubbard model. Moreover, recent NMR measurements [4] yield $\alpha \approx 1.25$, in good agreement with our spectroscopic results.

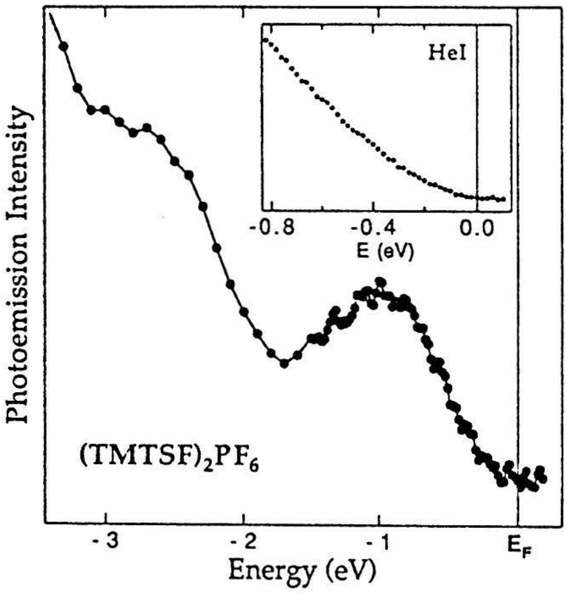

Figure 1 : He II photoemission spectrum of $(TMTSF)_2PF_6$ at T=50K. In the insert, the HeI spectrum near the Fermi level clearly shows, with a better statistics, that no Fermi edge is detectable and that the correlation exponent is larger than 1.

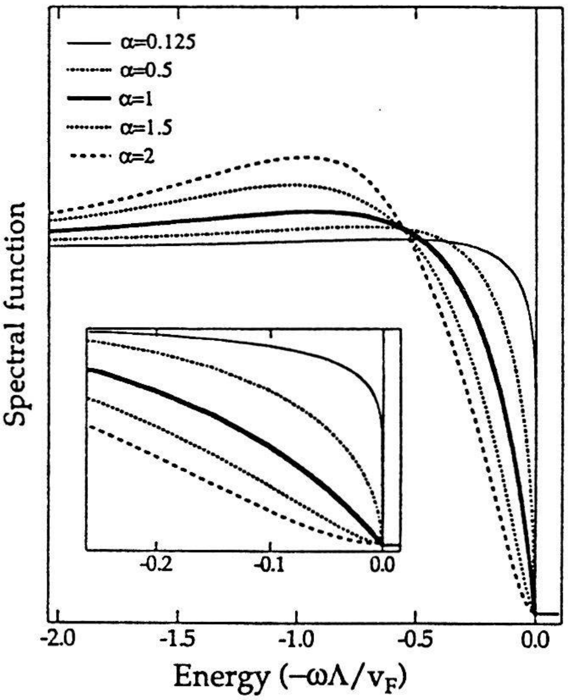

Figure 2 : Calculated spectral function of the Luttinger model for various correlation exponents α.

In conclusion, high resolution photoemission experiments on the metallic phase of $(TMTSF)_2PF_6$ show the absence of a Fermi edge. It is interpreted in terms of strong electronic correlations and support the Luttinger liquid picture with large power law exponent (α >1) value.

References :

[1] B. Dardel, D. Malterre, M. Grioni, P. Weibel, Y. Baer and F. Lévy, Phys. Rev. Lett. 67, 3144 (1991).
[2] K. Bechgaard and D. Jérome, Phys. scripta T39,37 (1991).
[3] S. Tomonaga, Progr. Theor. Phys. 5, 544 (1950). J.-M. Luttinger, J. Math. Phys. 4, 1154 (1963).
[4] P. Wzietek, F. Creuset, C. Bourbonnais, D. Jérome, K. Bechgaard and P. Batail, J. Physique I (France) 3, 171 (1993).

SPECTROSCOPIC ELLIPSOMETRY OF FeSi FILMS

M. Patrini and F. Marabelli
Dipartimento di Fisica "A. Volta", Via Bassi 6, I-27100 Pavia

N. Onda and H. Von Känel
Laboratorium für Festkröperphysik, ETH, CH-8093 Zurich

Spectral ellipsometry was used to characterize metallic FeSi films epitaxially grown on Si (111) by Molecular Beam Epitaxy. Measurements were performed in the 0.25-0.9 µm range on four samples of different thicknesses. Tg ψ and cos Δ spectra were analyzed in a multilayer model in order to determine the real and the imaginary part of the dielectric function of each sample. Differences between the spectra were attributed to strain effects, depending on the film thickness.

The synthesis of epitaxial iron silicides, in particular of semiconducting β-FeSi$_2$, has become of increasing interest in the last years both from a technological and fundamental point of view. Furthermore, epitaxial Fe silicides have come to be a model-system for the study of pseudomorphic growth, which occurs when large misfits between overlayer and the substrate exists. Structural investigations revealed that Fe$_{1-x}$Si films crystallizes in the cubic CsCl structure with a lattice constant close to half that of Si.

FeSi films of different thicknesses (50, 62, 350, 890 Å), with a Si cap layer of about 50, 20, 30 and 20 Å, respectively, were grown by room-temperature Molecular Beam Epitaxy (MBE) on (111) Si substrates. The 50 and 62 Å films without the Si cap layer are also available.

No chemical treatments on the surface of the samples were performed so the native oxide overlayers (SiO$_2$ or FeO$_x$) were taken into account by assuming a multiphase model in the data analysis, as explained below.

We measured FeSi optical response with a rotating polarizer spectroscopic ellipsometer SOPRA ES4G in the 0.25-0.9 µm spectral range. As it is well known, ellipsometry measures the complex ratio ρ of the reflection coefficients r_p and r_s (parallel and perpendicular to the plane of incidence, respectively), which can be expressed in terms of the amplitude ratio tg ψ and the phase difference Δ, as $\rho = r_p/r_s = \tan\psi\, e^{i\Delta}$.

The complex dielectric function $\varepsilon(\omega) = \varepsilon_1(\omega) + i\varepsilon_2(\omega)$ of the FeSi film can be derived from the measured tg ψ and cos Δ spectra adopting a multilayer structure, with sharp interfaces. In our case, the three phase-model (oxide-film-substrate) or the four-phase model (oxide-Si cap-film-substrate) were found to provide a consistent picture of the samples with or without the Si cap layer.

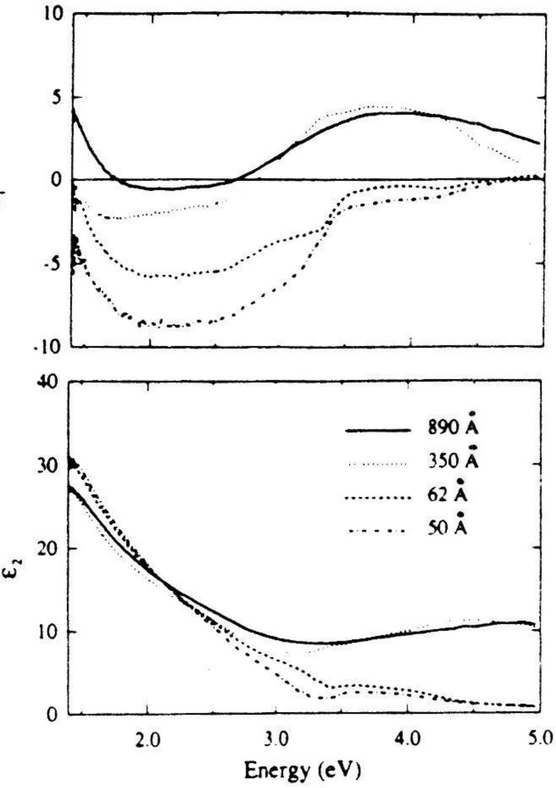

Fig.1 ε_1 and ε_2 spectra of FeSi films of different thicknesses.

In order to achieve an accurate determination of $\varepsilon_1(\omega)$ and $\varepsilon_2(\omega)$ of the FeSi films, we performed measurements at multiple angles of incidence (ϕ= 65°, 70°, 75°). The Si cap layer grown on the silicide has revealed to be amorphous Si and not crystalline Si, as expected, while the oxide layer has been quoted in 10-20 Å for all the samples.

The weak dependence of the optical functions on the angle of incidence for the thinnest films can be partially attributed to the the compressive strain, which was measured to decrease as the thickness of the film increases [3], so producing optical anisotropy.

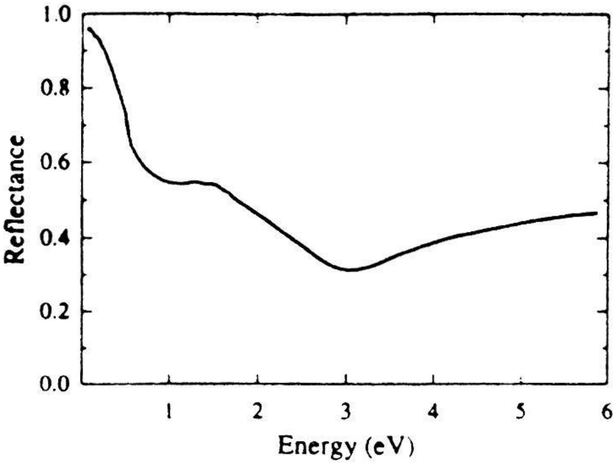

Fig.2 Reflectance of the 890 Å-sample.

The $\varepsilon_1(\omega)$ and $\varepsilon_2(\omega)$ spectra of all the samples are shown in Fig.1. In Fig.2 the reflectance spectrum of the 890 Å sample from 0.01 to 6 eV measured by a FTIR and a UV-vis spectrometers shows two different regions typical of a metal: a high reflectivity region due to intraband (free-carrier) transitions, followed by a minimum near 3 eV, roughly corresponding to the energy of the free-carrier hybrid resonance, screened by the interband transitions. At higher energies the interband transitions become dominant and the reflectivity increases again.

As regards the 890 Å and the 340 Å films, the experimental reflectance spectrum well agrees in the overlapping spectral range with that derived from ellipsometry. This confirms the multilayer model chosen for the thicker samples, while for the thinnest films the agreement is not so good. In fact, the inversion of the ellipsometric spectra to obtain $\varepsilon_1(\omega)$ and $\varepsilon_2(\omega)$ is extremely sensitive both to variation of the layer thickness of the order of few monolayers and to the type of amorphous Si chosen to simulate the Si cap layer.

The ε_1 and ε_2 spectra in Fig.1 show a marked dependence of both interband structures above 3 eV and screened intraband structures below 3 eV on the film thicknesses. Studies of absorption process in metal films [1,2] have shown that in the intraband region the increase of ε_2 above the intrinsic bulk value is the effect of surface roughness, while in the interband region the ε_2 spectra are determined primarily by void fraction, scattering by defects, grain boundaries or by internal strain.

In our case, structural investigations by STM, RHEED and XRD [3] have excluded the presence of surface roughness of the order of the incident wavelenght and of internal void fraction, confirming the good quality of the samples. The differences we note in the ε_1 and ε_2 spectra should be attributed mainly to internal strain, which can be effective in broadening, lowering and shifting the structures. The analysis of these effects requires not only the determination of the strain but also of the electronic bands involved in the optical transitions. In fact, it is well known that in metal silicides the electronic bands above and below the Fermi level strongly depend on the hybridization of the d(metal)- and p(Si)-levels that display different behavior in presence of internal strain.

REFERENCES

[1] D. Aspnes, E. Kinsbron and D. Bacon, Phys. Rev. B 21, 3290 (1980).
[2] P. Winsemius, H.P. Lengkeek and F.F. Van Kampen, Physica 79B, 529 (1975).
[3] N. Onda, H. Sirringhaus, S. Goncalves-Conto, C. Schwarz, E. Müller-Gubler and H. Von Känel, Mat. Res. Soc. Symposium Proceedings, in press.

Magnetooptical Kerr Effect Measurements with Picosecond Resolution

D. Guarisco, S. Frank, H. Hepp, and F. Meier

Laboratorium für Festkörperphysik, ETH Hönggerberg, CH-8093 Zürich

We have performed magnetooptical Kerr effect measurements with a pulsed high intensity dye laser. The pulse duration is 30 ps. A S/N ratio of 10 per pulse is achieved. In a pump-probe experiment, the change of the Kerr signal has been measured as a function of the delay between the probing and the heating pulses.

The spin-lattice relaxation time $\tau_{s\ell}$ has been measured for Gd, in a pump-probe experiment using time resolved spin-polarized photoemission with a pulsed laser as light source [1]. Information on $\tau_{s\ell}$ is also obtained from a time resolved measurement of the magnetooptical Kerr effect. The Kerr effect describes the change of polarization of the light upon reflection from a magnetic material.

In our experimental set-up the polar Kerr effect geometry is used. The high intensity, short (30 ps FWHM), gaussian shaped laser pulse of a dye laser (λ = 577 nm) is divided into a probing pulse and a heating pulse by a beam splitter. The time delay between the two pulses is adjusted (over a range of about 700 ps) by moving a prism. The probing pulse goes through a polarizer and is then focused on the sample. It impinges on it at an angle of 9°. After reflection it passes through a defocusing lens and an analyzer and it is detected with a PIN-photodiode. To compensate for the energy fluctuations of the laser pulses, a small fraction of the pulse energy is measured by a second photodiode as a reference. The heating pulse is focused on the sample under an angle of incidence of 40°.

The measured quantity is the Kerr ratio R, defined as $I(M_S)/I(-M_S)$, i.e., as the ratio between the signal at opposite magnetization directions, where $I(-M_S)$ has been mimimized by rotating the analyzer. M_S is the saturation magnetization. Since the sample has a rectangular hysteresis curve the measurements are done in remanence. The polarizer angle has been chosen such that the reflected light is linearly polarized for $-M_S$. Therefore it can be almost totally extinguished by the analyzer. At this optimum setting of the polarizer the Kerr ellipticity is compensated for by the ellipticity due to the metallic reflection. The polarizer is set at an angle of about 3° with respect to the s-direction. Accordingly, the light before reflection is approximately s-polarized. It follows that $I \propto (\alpha_K^2 + \varepsilon_K^2)$, where α_K (ε_K) is the Kerr rotation (ellipticity).

The Kerr signal is proportional to the intensity of the light. The Kerr ratio becomes an accurately measureable quantity provided that the background noise is kept sufficiently low. It is therefore important to eliminate as much as possible of the scattered light from the heating pulse. This is done by putting stops into the path of the measuring pulse and by putting a third polarizer into the path of the heating pulse such that the scattered light is extinguished by the analyzer.

Fig. 1 shows a hysteresis curve measured with one laser shot per point. For this curve the probing pulse alone was used. As can be seen, a S/N ratio of 10 is achieved. The sample was an evaporated a-$Tb_{21}Fe_{79}$ film (thickness 800 Å, substrate: glass, 1 mm thick), covered with 300 Å of SiO_2.

In Fig. 2 a time-resolved measurement is shown. The Kerr ratio is plotted against time. The curve was measured with 50 laser pulses per point. The sample consisted of an a-$Tb_{4.5}Gd_{17}Fe_{78.5}$ film (thickness 1073 Å) illuminated through ca. 1 mm of SiO_2 substrate and covered at the opposite side with 213 Å of Al.

Knowing the laser parameters, the lattice temperature profile during the laser pulse can be calculated [2].

For the spin-lattice energy interchange we assume the following model [3]:

$$\frac{dT_{\text{spin}}}{dt} = \frac{1}{\tau_{s\ell}}\left(T_{\text{lattice}} - T_{\text{spin}}\right).$$

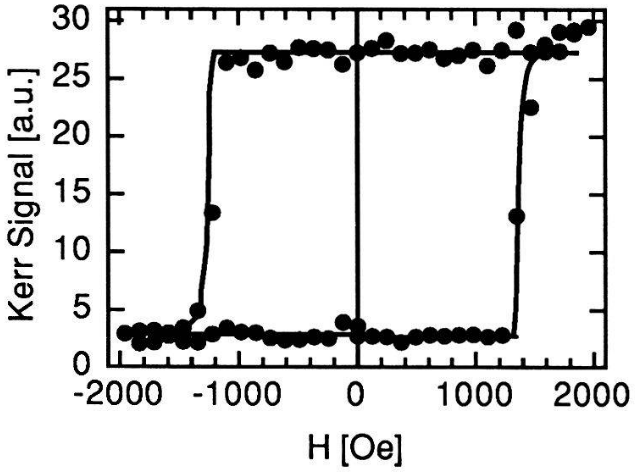

Fig. 1 Kerr effect hysteresis. Measuring pulse: laser energy= 286 nJ, $r_{1/e}$= 36 μm. T= 90°C. The solid line is a cw-Kerr measurement.

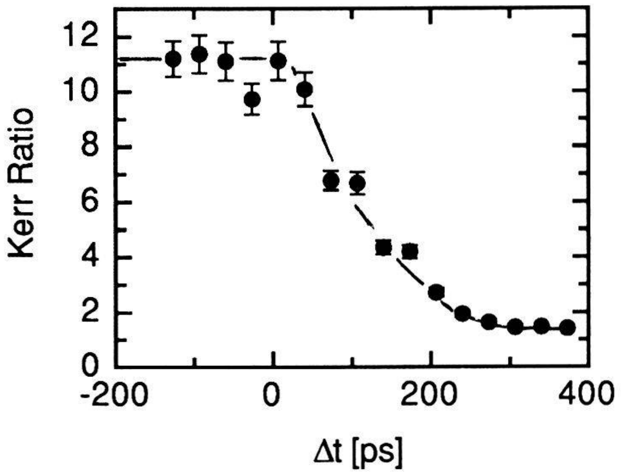

Fig. 2 Time-resolved Kerr effect measurement. Measuring pulse: laser energy= 0.1 μJ, $r_{1/e}$= 19 μm. Heating pulse: laser energy= 8.3 μJ, $r_{1/e}$= 120 μm.

By solving the above equation (either numerically or by using an analytical approximation for the lattice temperature) we get the temperature of the spin system. Then, from a curve of the magnetization vs. temperature, one can fit the measured Kerr curve and determine $\tau_{s\ell}$.

We thank E. Kay (IBM, Yorktown Heights) and P. Hansen (Philips Forschungslaboratorium, Aachen) for supplying the samples, and H.-C. Siegmann for his continuous support. The technical assistance of K. Brunner was crucial for the successful completion of the experiment. The financial support by the Schweizerische Nationalfond is gratefully acknowledged.

References

[1] A. Vaterlaus, T. Beutler, and F. Meier, Phys. Rev. Lett. **67**, 3314 (1991).
[2] J.H. Bechtel, J. Appl. Phys. **46**, 1585 (1975).
[3] S.I. Anisimov, B.L. Kapeliovich, and T.L. Perel'man, Sov. Phys. JETP **39**, 375 (1974).

Investigation of chromophore orientation of 2-docosylamino-5-nitropyridine and derivatives by nonlinear optical techniques

M. Küpfer, Ch. Bosshard, M. Flörsheimer, T. Borer, and P. Günter
Institute of Quantum Electronics, ETH Hönggerberg, CH-8093 Zürich
Q. Tang and S. Zahir
Ciba-Geigy AG, CH-4002 Basel

2-docosylamino-5-nitropyridine (DCANP) is a molecule displaying strong nonlinear optical effects in Langmuir-Blodgett (LB) films. DCANP shows higher nonlinearities as compared to its aliphatic chain derivatives ($C_{18}H_{37}$ to $C_{26}H_{53}$). To explain this we determined the orientation of the chromophores and the hyperpolarizabilities by means of nonlinear optical techniques.

Surface second-harmonic generation has emerged as a new technique to study surfaces and to determine the orientation of molecules on solid or water surfaces [1]. We used this technique to study Langmuir-Blodgett (LB) films of 2-docosylamino-5-nitropyridine (DCANP) [2] and derivatives on solid substrates.

The orientation of the charge transfer axis of a single molecule on a substrate can be defined by two angles θ and Φ (Fig.1). For more than one layer θ and Φ correspond to an average charge transfer axis. Since the hyperpolarizability of the amino nitropyridine derivatives treated here is highest along the charge transfer axis ξ, only $\beta_{\xi\xi\xi} =: \beta$ is considered. If all the intermolecular contributions to the nonlinear process are neglected d_{ijk} and β can be connected using the oriented gas model (assuming a δ-distribution of the orientation of the molecules) [3,4]

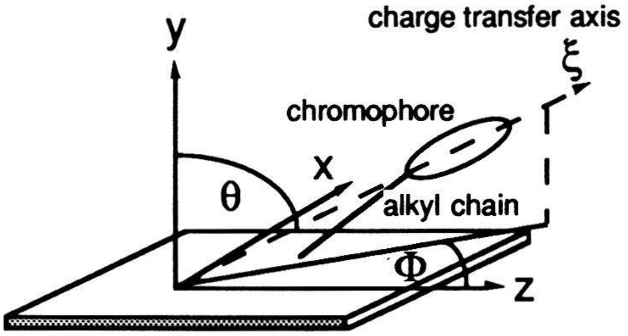

Fig.1: Orientation of a single DCANP molecule with respect to the substrate.

In our experiments the sample was rotated around various axes and the polarization of the fundamental and frequency-doubled beam was changed. The measured second-harmonic intensity $I^{2\omega}$ could be used to gain information on the orientation of the nonlinear optically active part of the molecules (the chromophore). Assuming a Dirac δ-distribution for the orientation of the molecules, θ and Φ could be obtained from

$$\theta = \arcsin\left[\left(\frac{d_{32}}{d_{31} + d_{33}} + 1\right)^{-1/2}\right] \tag{1}$$

$$\Phi = \arccos\left[\left(\frac{d_{31}}{d_{33}} + 1\right)^{-1/2}\right] \tag{2}$$

The measurements were carried out using a Nd:YAG laser operating at $\lambda = 1064$ nm with a repetition rate of 3 Hz and a pulse length of 25 ns. The beam with a pulse energy of 150 mJ was focused to a diameter of about 2 mm leading to an intensity of about 150-200 MW/cm^2 on the sample. The sample was mounted on a rotation stage which could be turned with a resolution of 0.01°. The measurements were performed with LB films of the amino nitropyridine derivatives C_nH_{2n+1}-NH-C_5H_3-NO_2. The film thickness was always 40 layers. In Table 1 we compare the results for the 5 derivatives.

Table 1: The nonlinear optical coefficients d_{33}, d_{31}, and d_{32} (in pm/V), the orientation angles θ and ϕ (in deg) and the hyperpolarizability β (in 10^{-40}m^4/V) for the nitropyridine derivatives examined.

Substance	d_{33}	d_{31}	d_{32}	θ	Φ	β
$C_{18}H_{37}$-NH-C_5H_3-NO_2	5.8	2.7	2.5	61	34	30
$C_{20}H_{41}$-NH-C_5H_3-NO_2	4.8	1.5	1.9	61	29	28
$C_{22}H_{45}$-NH-C_5H_3-NO_2	7.6	2.0	2.6	63	27	31
$C_{24}H_{49}$-NH-C_5H_3-NO_2	4.2	0.7	1.8	59	22	17
$C_{26}H_{53}$-NH-C_5H_3-NO_2	3.4	0.5	1.3	60	18	12

The angle θ (Fig.1) is nearly the same for all derivatives. The angle Φ, however, decreases with increasing carbon chain length indicating a better alignment of the chromophores with respect to the dipping direction. The largest nonlinear optical coefficient d_{33} has its highest value for DCANP. Probably this results from the superposition of two counteracting influences. The improving molecular alignment with increasing chain length and likely a decrease of the molecular nonlinear optical activity (e.g. due to local field effects of intermolecular interactions) for longer chain derivatives.

In conclusion we have shown that slight changes in the hydrophobic part of a LB film may significantly influence the orientation of the hydrophobic part and the associated nonlinear optical material parameters.

References

[1] Y.R. Shen, Nature **337**, 519 (1989).

[2] G. Decher, B. Tieke, C. Bosshard and P. Günter, J. Chem. Soc., Chem. Commun., 933 (1988).

[3] J.G. Bergman and G.R. Crane, J. Chem. Phys., **60**, 2470 (1974).

[4] J. Zyss and J.L. oudar, Phys. Rev. A, **26**, 2028 (1982).

Absolute Sign Determination of Nuclear Quadrupole Couplings by Laser - Radiofrequency Double Resonance

Dieter Suter and Tilo Blasberg

Institute of Quantum Electronics, ETH Zürich, CH-8093 Zürich

The combination of optical and radio frequency is a well-known technique for obtaining spectra of nuclear quadrupole transitions with high resolution and high sensitivity. A new and attractive feature of this technique is, that it allows not only the determination of the strength and orientation of the quadrupole- and Zeeman tensors, but also of the absolute sign of the nuclear quadrupole interaction. This determination of the sign, which is essential for the comparison with calculated EFG tensors, is not possible with purely magnetic methods.

The interaction between the quadrupole moment of nuclear spins and the electric field gradient tensor at the site of the nucleus, known as the quadrupole coupling, shifts the energy of nuclear spin states when the environment of the spins has less than cubic symmetry. The magnitude of this shift depends sensitively on the structural details of the environment and can provide information on average static structure, but also on crystal imperfections or dynamical processes. The measurement of nuclear quadrupole coupling constants is therefore an important tool of solid state physics. The measurements are usually performed by magnetic resonance techniques, which allow precise determinations of the coupling constants and therefore of the electric field gradient tensors. However, they provide only the absolute value of the coupling constant, but are insensitive to the sign of the coupling as long as the high temperature approximation for the spin system holds [1]. The same limitations apply to spectral hole-burning, an alternative method for the determination of quadrupole coupling constants [2]. Nevertheless, a combination of spectral hole-burning and laser-rf double-resonance technique [3] can provide information on both the absolute value and the sign of the nuclear quadrupole coupling.

Figure 1 shows schematically the principle of this method, which we call two beam Raman heterodyne spectroscopy. Our model system consists of three nondegenerate spin states in the electronic ground state and a single electronically excited state. In (1a), a pump laser beam at frequency ν_P saturates the transition from ground state sublevel |0> to the electronically excited state |e>. This spectral hole-burning process excites nonthermal populations of the spin states, whose sizes depend on the relevant relaxation processes. The radiofrequency field, which is resonant with transition |1>↔|2>, converts this population difference $\rho_{22}-\rho_{11}$ into a coherence. As shown in figure 1b), we detect this coherence optically with a test laser-field at frequency ν_T, which has to be resonant with an optical transition from one of the two sublevels |1> or |2> to the excited state |e>. The laser field transforms the coherence from the NQR transition into an optical coherence at frequency $\nu_T \pm \nu_{12}$, which propagates in the same direction as the test laser-field. On the photodetector, the two fields interfere, producing a

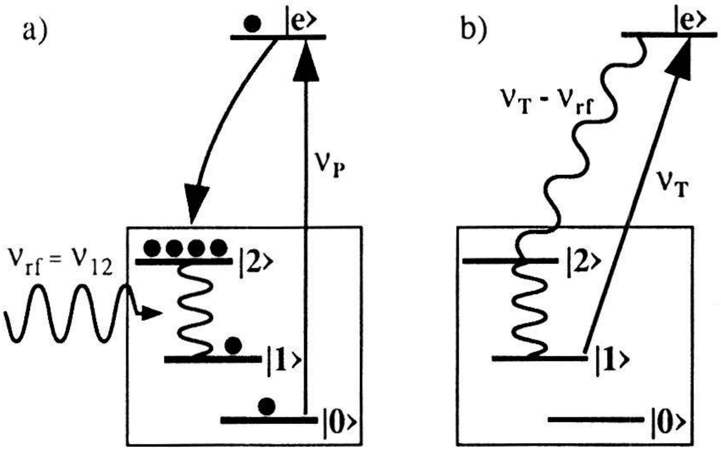

Figure 1: Principle of two beam Raman heterodyne spectroscopy

beat signal with frequency ν_{12}. The resulting signal depends resonantly on the detuning between the rf-frequency ν_{rf} and the NQR transition frequency ν_{12}. The laser frequency difference represents an additional parameter that allows the determination of the absolute sign of the coupling: the detection of the coherence is only possible, if the difference between the frequencies of the pump and test laser beams corresponds to an energy difference between two sublevels.

As an example, we have measured the nuclear quadrupole coupling of the impurity ion Pr^{3+} ($I= 5/2$) in the crystal host lattice $YAlO_3$ (YAP). Figure 2 shows schematically the experimental: two acoustooptic modulators shift the frequencies ν_P of the pump laser beam and ν_T of the test laser beam independently by up to ±30 MHz. The crystal is mounted on the cooling finger of a He flow-cryostat near a rf-coil, which is part of a tuned circuit. The beat signal between the laser- and the coherent Raman-field is detected with a photodiode and a lock-in amplifier.

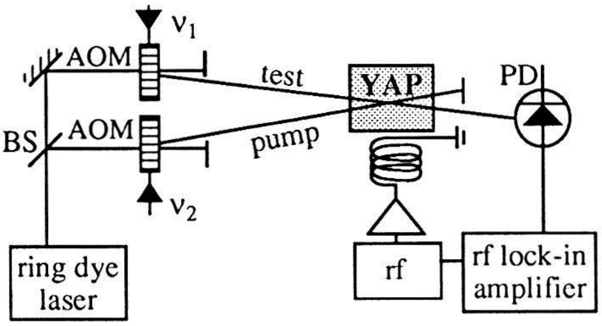

Figure 2: Experimental setup: BS = beam splitter, AOM = acousto-optic modulator, rf = radio-frequency synthesizer, PD = photodiode.

Figure 3a shows the observed signal as a function of the difference between the pump and test laser frequency. For this experiment, the rf-field was resonant with the transition between the spin states $m_I=\pm 1/2 \leftrightarrow m_I=\pm 3/2$ of the electronic ground state. Signal contributions are obtained, when the test laser-field frequency is resonant with the transition from one of the two sublevels |1> or |2> to the excited state |e> and the pump laser frequency with any of the three possible transitions. As shown in figure 3b, c), the five distinguishable frequencies are distributed asymmetrically. Comparison of the experimental spectrum with the two theoretical stick spectra shows clearly, that the quadrupole coupling in this case is negative.

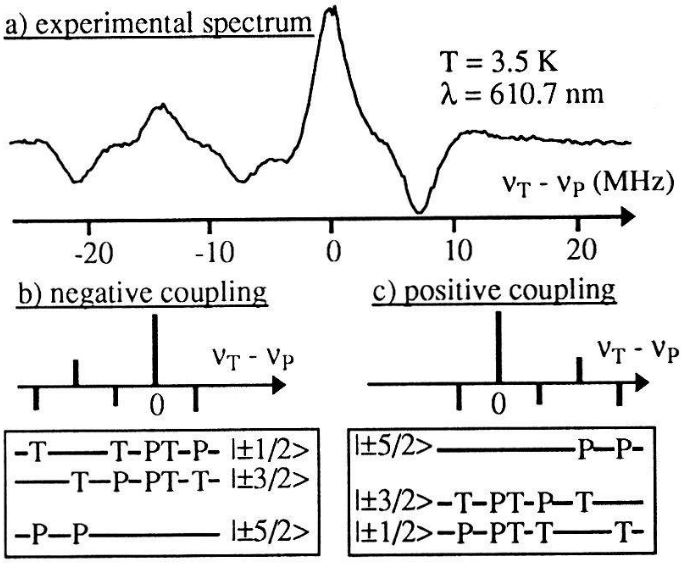

Figure 3: Experimental spectrum (top) compared to the calculated stick spectra

In conclusion, we have demonstrated, that both, the coupling constants and the absolute sign of the nuclear quadrupole interaction can be determined with a laser-radiofrequency double-resonance experiment.

This work was supported by the Schweizerischer Nationalfonds.

References

[1] A. Abragam, *The Principles of Nuclear Magnetism.*, Oxford University Press, Oxford (1961).
[2] S. Völker, Ann. Rev. Phys. Chem. 40, 499 (1989).
[3] N.C. Wong, E.S. Kintzer, J. Mlynek, R.G. DeVoe, and R.G. Brewer, Phys.Rev.B 28, 4993 (1983).

DEVELOPMENT OF AN ISOCHRONOUS TIME-OF-FLIGHT MASS SPECTROMETER FOR DETERMINATION OF SPACE PLASMA PARAMETERS

L. GUBLER[1], E. MÖBIUS[2] and P. BOCHSLER[1]
[1] Physikalisches Institut, Universität Bern, Sidlerstrasse 5, 3012 Bern
[2] Institute for the Study of Earth, Oceans and Space, University of New Hampshire, Durham NH03824

For plasma composition measurements in space, the usual magnet spectrometers are increasingly replaced by time-of-flight (TOF) instruments. We have developed a prototype for a cylindrical, high-resolution (M/ΔM>50) isochronous TOF-mass spectrometer, to be used in combination with an electrostatic energy-analyzer. We present numerical simulations and first experimental results.

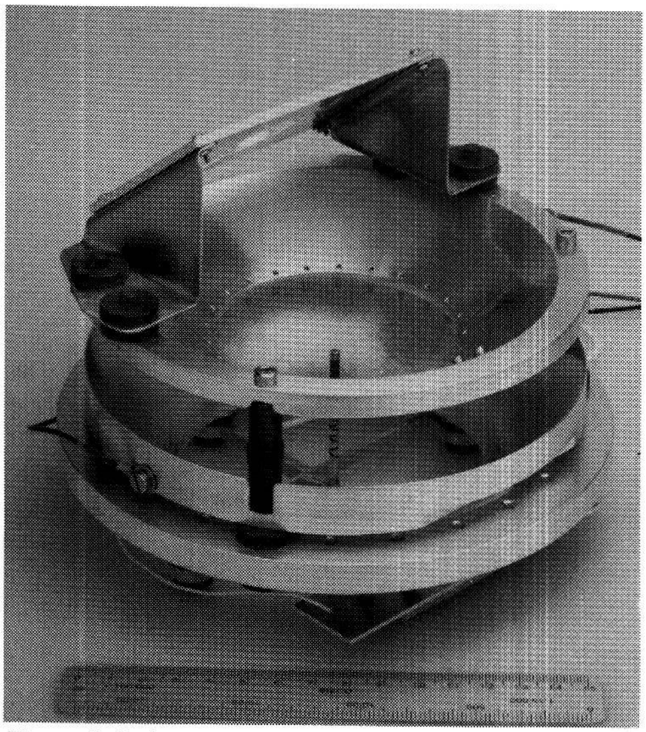

Figure 1: Laboratory prototype for a cylindrically symmetric time-of-flight instrument.

Since 1984 the time-of-flight technique has been successfully used in space applications for the determination of the plasma composition in various environments[1]. Instruments using this technique combine an electrostatic analyzer to select the incoming ions by their energy per charge ratio and a TOF-section, where the time between the passage through a thin entrance foil and the impact in a solid state detector is measured. Both events release electrons which are collected as start or stop signals. The information about the energy per charge and the velocity in the time-of-flight path yields the mass per charge ratio. Angular scattering and energy straggling of the ion in the foil usually limit the resolution of conventional sensors. To avoid this disadvantage, the application of isochronous time-of-flight sections with linearly increasing retarding electrostatic fields has been proposed[2]. In such instruments, the ions perform half of a harmonic oscillation and are reflected back into the plane of incidence. The time-of-flight is then independent of the energy and entrance angle of the ion. In that way, a much better resolution can be achieved, provided that the charge of the ion after the foil passage is known. In the keV/u-energy range this charge is for many elements typically 0 or +1. Thus, for deflected particles this charge will be +1 with a high likelihood.

If the potential is required to be a solution of Laplace's equation, it is sufficient to fix the boundary values in order to achieve an ideal field configuration. A potential with cylindrical symmetry, which increases quadratically, has the following general form:

$$\Phi(r, \vartheta, z) = aLog(r) - b(r^2 - 2z^2) + d \qquad (1)$$

The time-of-flight is given by:

$$T = \frac{\pi}{2}\sqrt{\frac{m}{b \cdot q}} \qquad (2)$$

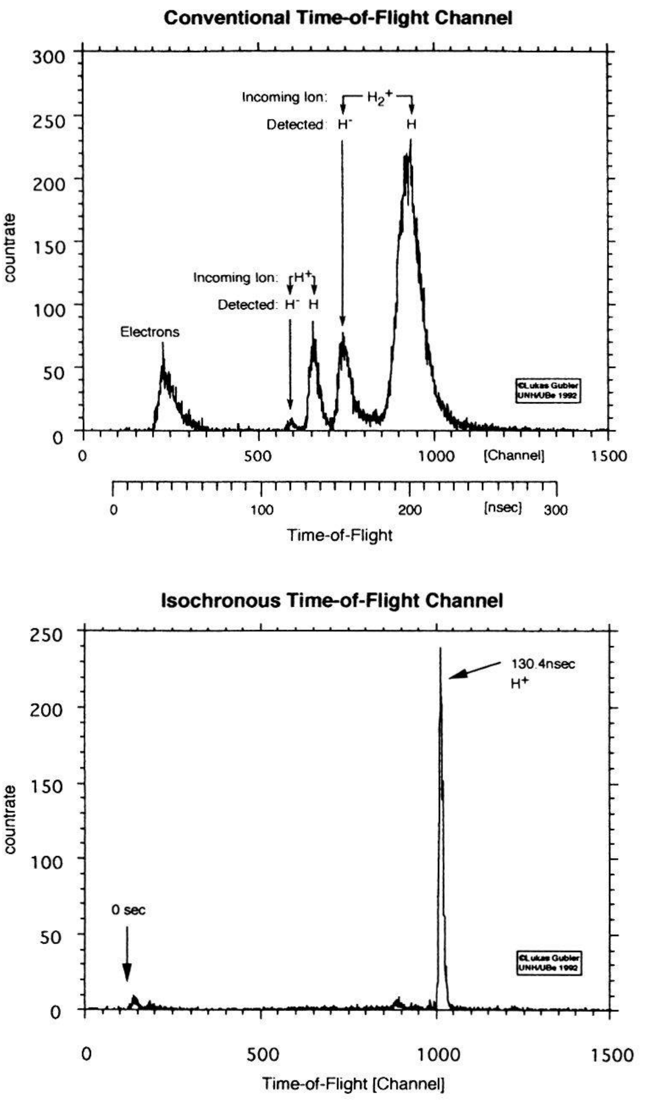

Fig.ure 2: Time-of-flight spectra for conventional and isochronous channel.

The penalty to be paid with the quadratic term in (1) is a strong defocusing of the ion trajectories. The logarithmic term, which corresponds to a superimposed cylindrical electric field, partly compensates the defocusing effect. The value of the parameters a, b and c can be optimized analytically. The influence of the non-ideal electrodes is estimated and minimized with a numerical simulation of the potential and a calculation of the ion trajectories.

In Fig. 1 we show a laboratory prototype which was developed to experimentally verify these properties. The potential is defined by a large MCP-detector in the ground plane, the outer ring electrode, a thin stick in the middle and the upper cup. Because the upper electrode mainly consists of a grid, it is also possible to analyze neutral particles emerging from the foil with an additional TOF-channel.

We have carried out some initial tests at the facility of UNH. In Fig. 2 we show a spectrum for hydrogen in the neutral channel. Depending on the nature of the primary ion, the atoms emerge from the foils with two distinctive energies. Negatively charged particles are also detected and have a slightly shorter time-of-flight because of the attracting electrostatic field. The singly charged ions show up as very sharp peak in the spectrum of the isochronous channel.

With this technology, it is also possible to distinguish for example between D^+ and H_2^+ or between $^{15}N^+$ and $^{12}CH_3^+$ and $^{14}NH^+$: Molecules penetrating a carbon foil break up into their constituents. Charged and neutral components are simultaneously detected in the two time-of-flight channels[3]. The neutral particle is used to measure the mass per charge ratio of the original molecule and the mass of the charged fragment is accurately determined in the isochronous channel. The background for the detection of molecules can be reduced to very low values, because triple coincidences will be employed.

The laboratory prototype was designed and built by R. Burckhalter and H. Schwab from the Ingenieurschule Biel in collaboration with J. Fischer. Financial support by the Swiss National Science Foundation is acknowledged.

1. Gloeckler, G., *et al.*, *The Charge-Energy-Mass Spectrometer for 0.3-300 keV/e Ions on the AMPTE CCE*. IEEE Trans. Geosci. Remote Sens., 1985. **GE-23**(3): p. 234-240.
2. Hamilton, D.C., *et al.*, *New high-resolution electrostatic ion mass analyzer using time of flight*. Rev. Sci. Instrum., 1990. **61**(10): p. 3104-3106.
3. Möbius, E., *et al.*, *High mass resolution isochronous time-of-flight spectrograph for three-dimensional space plasma measurements*. Rev. Sci. Instrum., 1990. **61**(11): p. 3609-3612.

HOW TO DETECT PLASMOIDS IN THE SOLAR CORONA?

R. NEUKOMM and P. BOCHSLER
Physikalisches Institut, Universität Bern, Sidlerstr.5, 3012 Bern, Schweiz

We examine in a model the movement of closed magnetized structures (plasmoids) in the solar atmosphere. We discuss the development of the ionisation state distributions of oxygen and silicon. Charge states of minor ions are generally important tracers for processes and conditions to which these particles were exposed. In the solar wind they carry information about the inner heliosphere which can otherwise not be derived from other quantities mesurable at 1 AU.

Magnetic reconnection is a common feature in heliospheric and magnetospheric physics. Configurations exist where a closed magnetic structure, called plasmoid, is formed. On the solar surface this can occur during a solar flare, or, in magnetospheric physics, in the progress of a magnetic substorm. In the solar atmosphere, a plasmoid can be ejected into the solar corona and can be driven up as a consequence of magnetic buoyancy in the diverging external magnetic field.

There are several phenomena in coronal physics which are not yet understood and which are possibly linked to the formation of plasmoids. The outstanding problem is the heating of the solar corona. Parker [1] estimated the heat input of nanoflares, i.e. small reconnection events, and found that they could supply sufficient energy to maintain the coronal heating process. Another open question is related to the origin of fluctuations in the solar wind. Observations show that the solar wind is far from being a steady-state phenomenon. Measurable quantities such as magnetic field strength, velocity, temperature, density and also charge state distributions of minor ions show fluctuations on very different spatial and temporal scales. Some of these can be followed back to events occuring on the solar surface. The fundamental question remains open whether one has to visualize the solar wind as a continuous particle flow, disturbed by events of the active sun, or if these fluctuations are an intrinsic property of the solar wind originating from discretes sources.

The model we took for describing the propagation of plasmoids is adapted from Cargill and Pneuman [2] for the special case of a magnetic pressure dominated plasmoid ($\beta \ll 1$). The equation of motion of a plasmoid in the solar atmosphere is:

$$\ddot{r} = -\frac{4}{m_{prot} n_{i0}} \left(p_{e0} + \frac{{B_{e0}}^2}{2\mu_0} \right)^{3/4} \frac{d}{dr} \left(p_e + \frac{{B_e}^2}{2\mu_0} \right)^{1/4} - \frac{\Gamma M_\odot}{r^2} \tag{1}$$

The terms on the right-hand-side describe the buoyancy due to thermal and magnetic pressures and the weight within the gravitational field of the sun.
The energy equation including heating and radition loss is given by:

$$\dot{T} = +\frac{3}{4}(\gamma - 1) T v \frac{d}{dr} \left[ln \left(\frac{{B_e}^2}{2\mu_0} + p_e \right) \right] + \frac{(\gamma - 1)}{2 k n_{i0}} (H - R_L) \left(\frac{p_{e0} + \frac{{B_{e0}}^2}{2\mu_0}}{p_e + \frac{{B_e}^2}{2\mu_0}} \right)^{3/4} \tag{2}$$

The heating could be due to slow reconnection of the plasmoid field with the ambient magnetic field. To maintain a pressure equilibrium between the plasmoid and the external solar atmosphere the following relationship was used:

$$B_i^2/2\mu_0 + p_i = B_e^2/2\mu_0 + p_e \qquad (3)$$

Furthermore, the conservation of magnetic flux inside the plasmoid was required:

$$B_i^2 R^2 = const = B_{i0}^2 R_0^2 \qquad (4)$$

Supplementary to Cargill and Pneuman we introduce the equations for the reactions rates for recombination and ionisation processes of hydrogen and one minor ion.[3]

We emphasize that the solution of the differential equations depends strongly on the initial conditions. For the following examples we assumed a start velocity of 10 km/s at an altitude of 2200 km with a plasma-β of 0.001 and a heating rate of 0.25 eV per particle and second. Solving the system of equations numerically leads to the ionisation states at 20 AU depicted in Fig. 1: The prefered charge state of oxygen is 4+ and remains almost constant until 1AU. The dominant charge state of silicon is also 4+.

Comparison with solar wind observations [4] shows a difference: The most abundant oxygen ion has charge state 6+. Similarly, observed ionisation states of silicon range from 7+ to 10+.

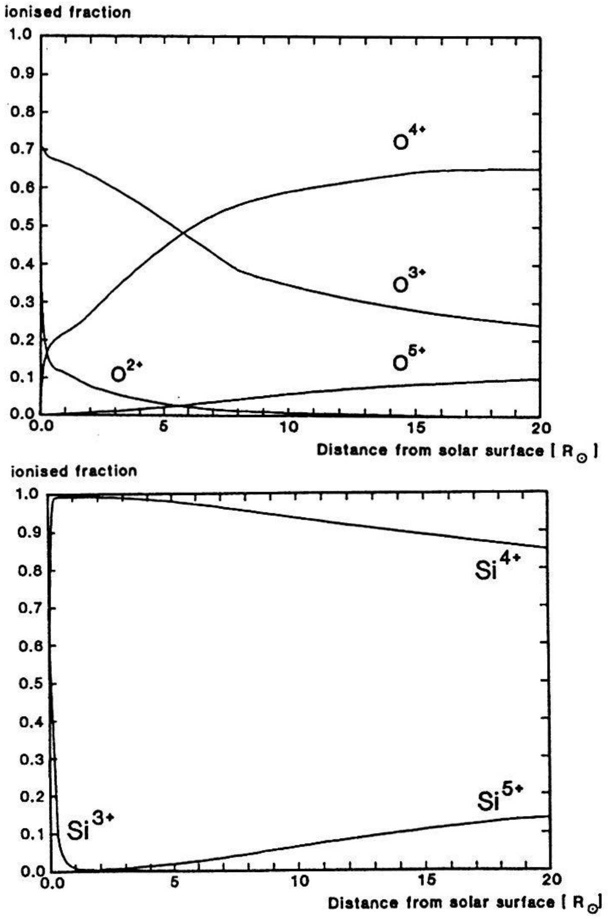

Fig. 1: Ionisation states of oxygen (top panel) and silicon (lower panel) according to the plasmoid model.

Despite of the dependence on initial conditions, there remains the qualitative conclusion that the content of a model plasmoid shows unusual minor ion charge state distribution compared to solar wind. If plasmoids exist similarly to the model and if they survive the journey through the lower corona, it should be possible to observe ionisation states different from typical solar wind conditions at 1AU. The duration of these events is expected to be a few minutes, depending on the plasmoids initial velocity and size. Unfortunately, the detection of such short-time events with presently flying instrumentation is difficult or even impossible.

We acknowledge financial support by the Swiss National Science Foundation.

References

[1] E.N.Parker, Astrophys.J. **330**, 474 (1988)
[2] P.J.Cargill and G.W.Pneuman, Astrophys.J. **276**, 369 (1984)
[3] R.Neukomm, Lizentiatsarbeit Universität Bern, in preparation, (1993)
[4] G.Gloeckler *et al.*, Astron. Astrophys. Suppl. Ser. **92**, 267, (1992)

PARAMAGNETIC OXYGEN DETECTION WITH AN ULTRASONIC RESONATOR

O. Oehler, P. Egli, P. Nizzola, H.P. Schneibel, M. Uebersax, C. Würgler

Institute for Quantum Electronics, Swiss Federal Institute of Technology,
CH-8093 Zurich, Switzerland

The presented method for the selective detection of oxygen is based on the measurement of periodic variations in the velocity of sound. These variations are induced in an oxygen-containing gas sample by the attraction of the paramagnetic oxygen molecules in a modulated inhomogeneous magnetic field. The variations in the velocity of sound are measured by detuning an ultrasonic resonator. At a modulation frequeny of the magnetic field of 20 Hz and a time constant of 1 s a S/N ratio of 47 was found.

The paramagnetism of oxygen allows to detect this gas in a highly selective manner [1]. There are several methods for using this property of the oxygen molecules. A well-known method is the measurement of the buoyancy of diamagnetic balls in a gas sample in the presence of an inhomogeneous magnetic field [2]. The oxygen contents of the sample gas leads to driving the balls out of the magnetic field. This method suffers from a low time constant because of the large inertia of the balls. Further methods are based on magnetic field induced gas movements or pressure variations [3]. Because of the small magnetic forces, these methods are highly sensitive to thermal and acoustic disturbances, respectively.

The dependence of the velocity of sound in an oxygen-containing gas on an inhomogeneous magnetic field and the accurate measurability of changes of this sound velocity with an ultrasonic resonator [4] offer the possibility of constructing a highly selective and sensitive oxygen detector.

The ultrasonic resonator cavity C consists of two identical transducers arranged opposite each other and at a distance of about 10 mm in a thermally isolated metal tube M (Fig. 1). The transducers (one used as an emitter E, the other as a receiver R) are tuned to an acoustic resonance at a frequency of 220 kHz (O_1). One of them is fixed to a piezo-driven actuator A. The phase of the received signal is compared (P) to the input signal. A signal proportional to the phase difference is used to control the actuator via a device Q which imposes a charge. This signal is fed to a digital storage oscilloscope D. An inhomogeneous magnetic field is additionally applied to the resonator cavity C. This field is established by coil B which is operated with the low frequency oscillator O_2 and by the anchor H with edged pole pieces.

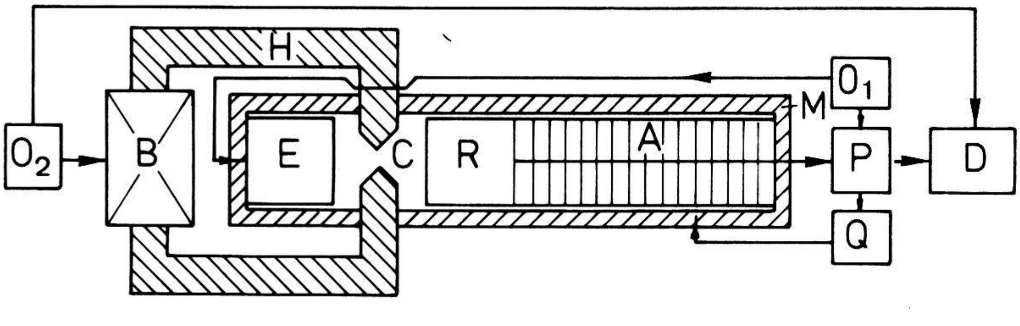

Fig. 1 Layout of the oxygen detector

The dependence of the velocity of sound on the magnetic field is given in Fig. 2. The upper half shows the variation of the magnetic field. The scale refers to the field maximum at the centre between the two pole pieces. In the lower half of Fig. 2 the amplitude of the velocity of sound is given. It is noteworthy that the velocity of sound variations were detectable at a resolution of 0.1 mm/s. As expected, the velocity of sound signal was found to be independent of the polarization of the field.

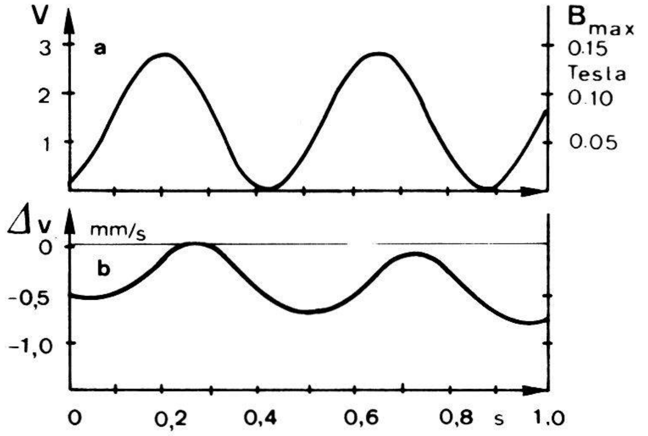

Fig. 2 Time evolution of the velocity of sound (b) as a function of the inhomogeneous magnetic field variations (a)

The frequency dependence of the velocity of sound is given in Fig. 3. The large decrease of the signal at a high modulation frequency of the magnetic field indicates that a complex mechanism governs the observed effect. At low frequency the effect has to be assigned to the periodic migration of the oxygen molecules into the magnetic field while at high frequency the effect is mainly controlled by pressure variations.

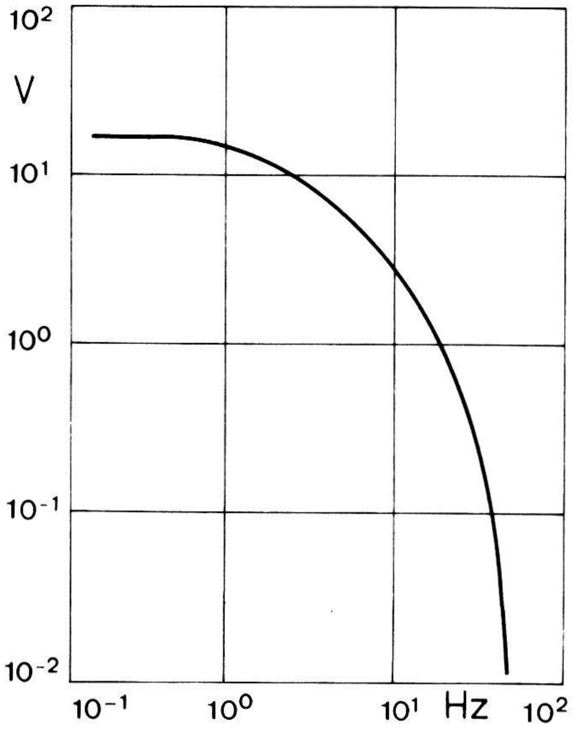

Fig. 3 Frequency dependence of the oxygen effect

As there are no moving parts in the device, the method allows to detect the oxygen concentration at a rather high frequency. Even at 20 Hz a signal/noise ratio of 47 was found at a time constant of 1 s.

The control of the magnetic field by a Hall sensor and the maintenance of the tuning of the ultrasonic resonator through changes of the gas composition are subject of present investigations.

We would like to thank the Swiss Energy Research Foundation NEFF and Landis & Gyr Building Control AG, Zug, Switzerland for supporting this project.

References

[1] P. Profos, "Handbuch der industriellen Messtechnik", Essen 1974.
[2] L. Pauling, RE. Wood, J. Am. Chem. Soc., **68**, 795 (1946).
[3] H. Hummel, , Chemie-Ing-Technol., **40**, 947 (1968).
[4] O. Oehler, J. Wieland, D. Raillard and M. Schumacher, Springer Series in Optical Sciences, III, Vol. **69**, p. 240 (1992).

Fractal Analysis of Development of Twin Domains in Thin Films

G. Gerth, S. Grosse, M. Krohn† and H. Haefke‡
Max Planck Institute of Microstructure Physics, Weinberg 2, D-O-4050 Halle (Saale);
† D-O-4070 Halle (Saale), Murmanskerstrasse 9;
‡ Institute of Physics, University of Basel, Klingelbergstrasse 82, CH-4056 Basel

Complete (111) epitaxy of thin films of f.c.c. materials on mica cleavage faces implies the formation of twin domains as a consequence of double-positioned nucleation of islands. The development of the twin domains in AgBr thin films on mica is studied by methods of fractal analysis.

Electron microscopy replica techniques reveal the formation of twin domains in (111)-oriented AgBr thin films grown on mica(001) via 3D nucleation and coalescence of islands during vapour deposition in ultrahigh vacuum [1]. The twin boundaries become apparent by their grooves on the film surface as shown in Fig. 1. In contrast to grain boundaries in polycrystalline thin films, the domain boundaries exhibit no triple points rather they are characterized by a fractal structure.

We have measured the total length of the boundary lines per unit area S_l (cm/cm^2) with a given scale length l for various substrate temperatures and film thicknesses and have traced it in fractal plots [2,3] as given in Fig. 2. The decrease of the measured line length S_l with increasing scale l is characterized by three regions of different slope $p = 1 - D$ in a double logarithmic plot separated by well-defined kinks l_1 and l_2. Region II (with a fractal dimension of $D = 1.30$ nearly equally for room temperature (RT) and 100 °C) reflects the ripple of the boundary lines due to the grouping of equally positioned islands to larger domains. Region I (with $D = 1.70$ nearly equally for RT and 100 °C) reflects the statistics of the domain distribution in a large scale. The fractal behaviour ends at l_2. In region III the measured S_l is independent of the scale l and can be regarded as the true density of lines S_0 (cm/cm^2. We define a mean domain size q (cm) by regarding the irregular boundaries as being arranged in equidistant straight lines with distance $q = 1/S_0$. Thus, it turns out that $l_1 = 1.3 \times q$ and $l_2 = 0.35 \times q$ for RT and 100 °C, respectively (cf. Fig. 2). This suggests that both curves reflect the same fractal phenomenon, with the RT curve being shifted upwards and to smaller scales exclusively due to the smaller domain size q. Indeed, it turns out that the two curves fit fairly well in a normalized fractal plot of log $(S_l/S_0$ *vs.* log $(1 \times S_0)$.

Figure 3 shows the domain size q, determined as described above, to increase with increasing film thickness for 100 °C while it is rather constant at RT. The observed domain growth at higher substrate temperature is a result of a thermally induced and capillary driven motion of domain boundaries.

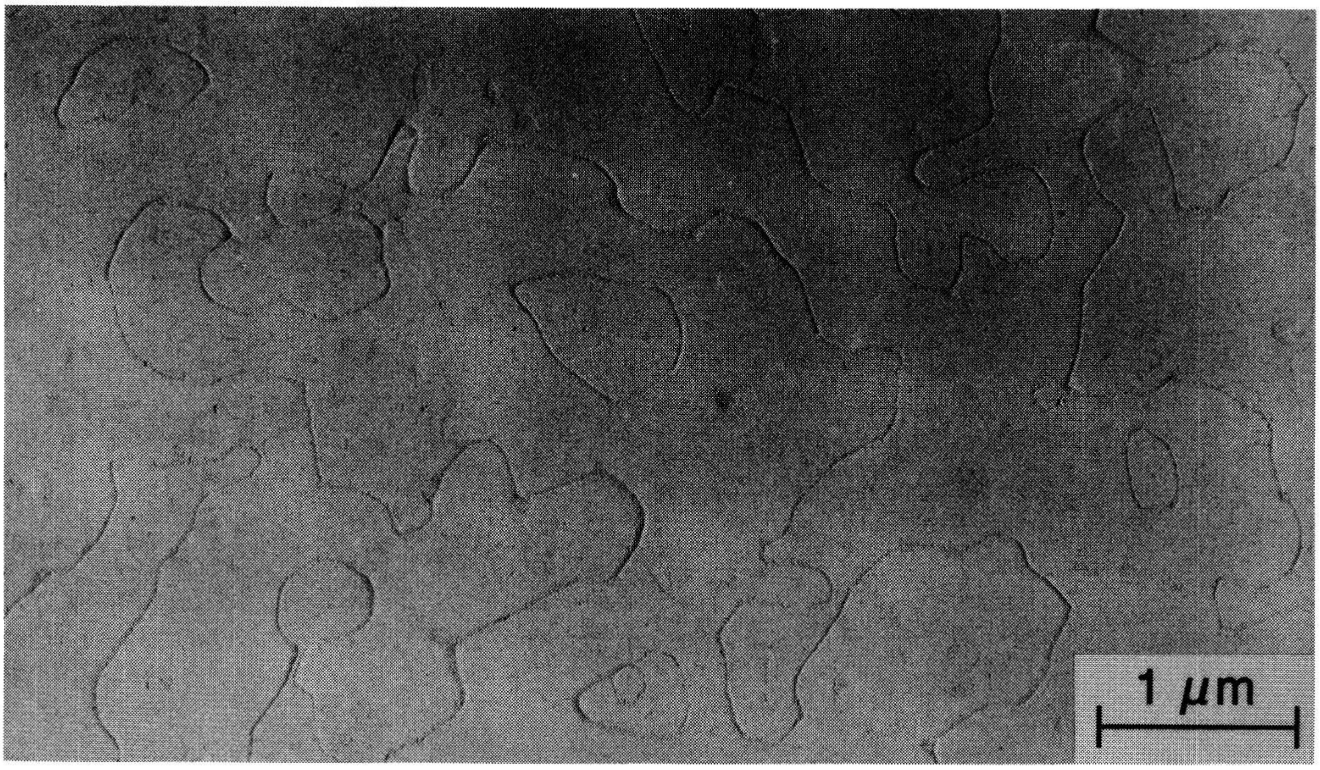

Fig. 1: Twin domains on a 200 nm thick AgBr film vapour-deposited on mica at room temperature. TEM replica technique.

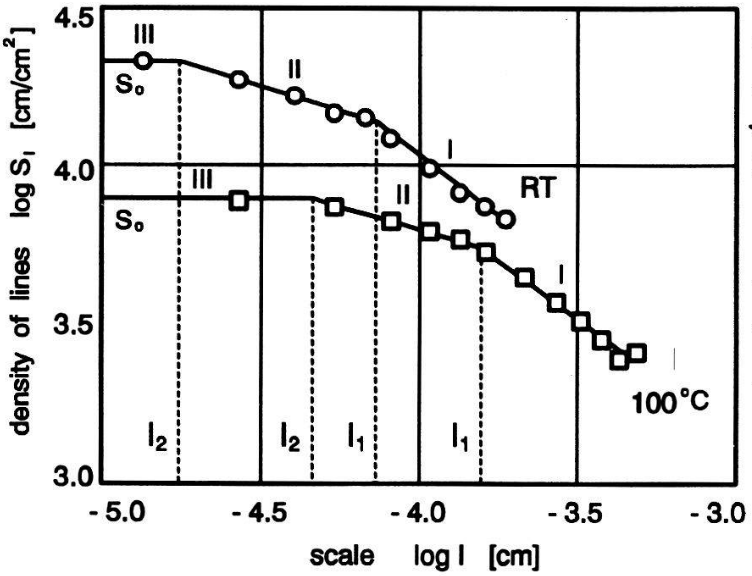

Fig. 2: Double log plot of measured total length of twin boundaries per unit area S_l versus applied scale length l, for 50 nm thick AgBr film on mica.

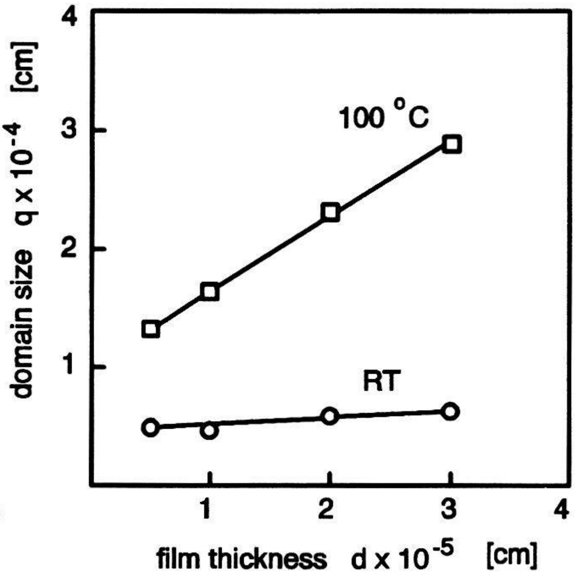

Fig. 3: Domain size q determined for AgBr on mica for RT and 100 °C in dependence on film thickness.

References

[1] G. Gerth, M. Krohn, L. Howald and H. Haefke, Helv. Phys. Acta **65**, 876 (1992).
[2] B.B. Mandelbrot, *The Fractal Geometry of Nature* (W.H. Freemann, San Francisco, 1982).
[3] J. Fricke, Phys. Zeit, **17**, 151 (1986).

Cross Section and Analyzing Power A_y for the D($\vec{\text{p}}$,pp)n Break-up Reaction at 65 MeV in the QFS Configuration

M.Allet*, K.Bodek*, W.Hajdas*, L.Jarczyk†, St.Kistryn†, J.Lang*, R.Müller*, S.Navert*, O.Naviliat-Cuncic*, J.Smyrski†, J.Sromicki*, A.Strzałkowski†, J.Zejma*

* Institut für Mittelenergiephysik, Eidgenössische Technische Hochschule, Zürich
† Institute of Physics, Jagellonian University, Cracow

The differential cross section and the analyzing power A_y were measured for the D($\vec{\text{p}}$,pp)n breakup reaction at a beam energy of $E_{\vec{p}}$ = 65 MeV in the symmetrical Quasi Free Scattering (QFS) configuration ($\vartheta_1 = 44°$, $\vartheta_2 = 44°$, $\varphi_{12} = 180°$). Experimental set-up, results and their comparison to the Fadeev calculations are presented.

A study of the 3N-system may provide information on 2N-potentials which is hardly available (or not available at all) from 2N-systems. In order to achieve a consistent description of the 3N-system it is, however, necessary to know the role of genuine 3N-forces in the dynamics of the 3N-system. The aim of this study was to measure the differential cross section and the analyzing power A_y in the QFS configuration and compare it with rigorous Fadeev calculation . This configuration is supposed to reveal only a weak sensitivity to the effects of 3N-forces and the amplitude is dominated by the 2N-interaction. It is interesting to verify to what extend calculations with realistic 2N-potentials, but without 3N-forces, can reproduce the experimental data.

The proton beam with an energy of 65 MeV, a polarization $|P_y| \approx 0.8$ and a current of about 250 nA from the Philips injector cyclotron of the Paul Scherrer Institute impinged onto a deuterium gas target cooled to 77 K. Two plastic scintillator (NE102) ΔE-E telescopes set at $\vartheta_1 = 44°$, $\vartheta_2 = 44°$, $\varphi_{12} = 180°$ were used to detect charged reaction products. Fast electronics and the on-line data aquisition system selected p-p coincidences. The collimating system was designed to allow for a normalization by means of the elastic p-d cross section. For this purpose, the elastically scattered particles were collected simultaneously with a reduced rate. Time-of-flight information, with respect to the RF-signal of the cyclotron, was recorded as well. The coincidence width was chosen such that events from two subsequent beam burst were accepted. This method provides a clean subtraction of random coincidences in the off-line analysis. The energy calibration of the telescopes was obtained from a measurement of elastically scattered protons at different angles in a separate run.

In the off-line analysis two dimensional energy spectra of p-p coincidences were built. The recoil deuterons were discriminated (ΔE-E method) and random coincidences were subtracted. The events around the 3-body kinematical locus were projected onto the central kinematical curve. The energy bin was 2 and 4 MeV for the cross section and analyzing power, respectively. The value of the elastic pd-cross section used in the normalization procedure was taken from ref [1].

The rigorous Fadeev calculations using four realistic potentials (Argonne v_{14}, Bonn B, Nijmegen, Paris) were performed by the Bochum-Cracow group [2]. The maximal total angular momentum of the 3N-system included was $j_{max} \leq \frac{25}{2}$ whereas the maximal total angular momentum of the 2N-subsystem was $J_{max} = 3$. Before the comparison with the experimental data the theoretically calculated observables were folded with the experimental resolution function by a Monte Carlo technique. The resulting theoretical spectra were projected onto the kinematical curve with the same method as applied for the experimental data. The result is shown in fig.1. A very good agreement of the absolute value of the cross section in the maximum of the QFS-peak was found for three potentials (Argonne v_{14}, Bonn B, Nijmegen) but the predicted width is bigger by 15 %. This may be due to Coulomb effects. The calculations aiming in a verification of this hypothesis are under way [3].

References

[1] H.Shimizu, K.Imai, N.Tamura, K.Nisimura, K.Hatanaka, T.Saito, Y.Koike and Y.Taniguchi, Nucl. Phys. **A382** (1982) 242

[2] H.Witała, W.Glöckle and Th. Cornelius, Few-Body Systems **6** (1989) 79

[3] W.Glöckle, H.Witała and J.Golak, private communication

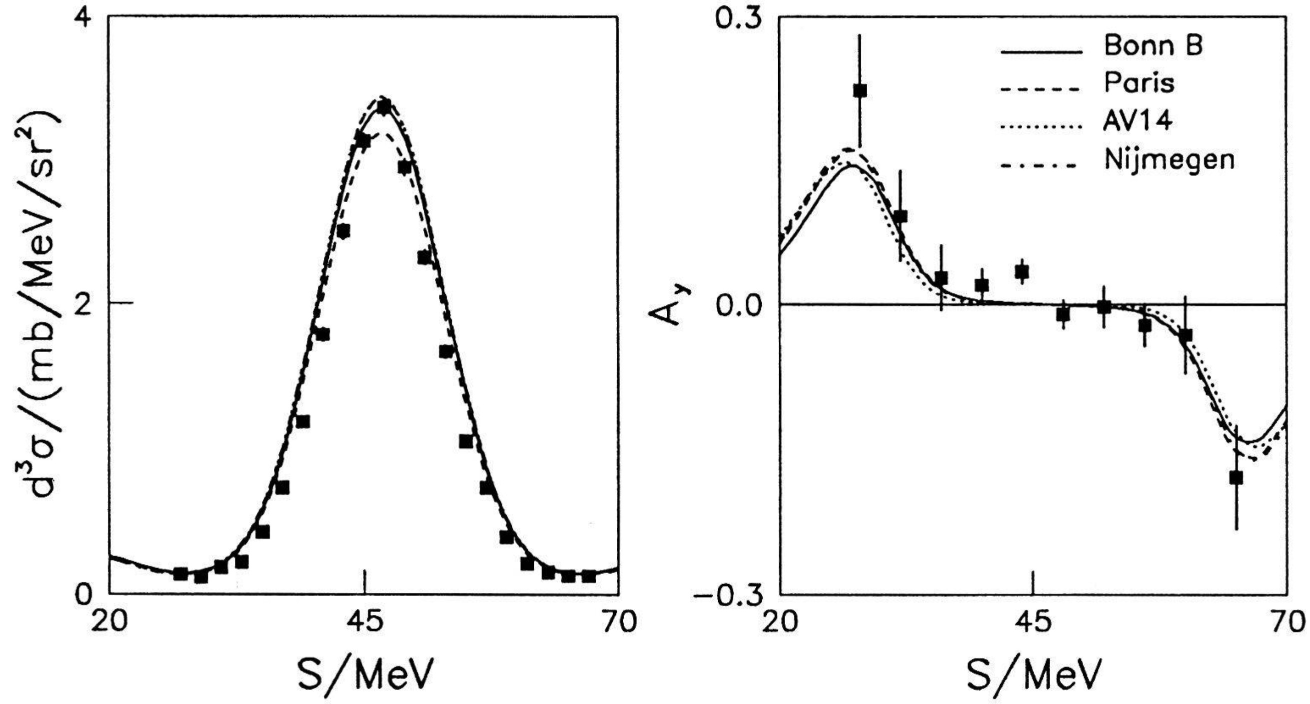

Fig.1. The cross section and the analyzing power A_y for the QFS configuration ($\vartheta_1 = 44°$, $\vartheta_2 = 44°$, $\varphi_{12} = 180°$) - the experimental results and the Fadeev calculations using realistic potentials.

Muon Capture Ratios A(H/Ne) in Gaseous Mixtures of H_2 + Ne

A. Werthmüller, R. Jacot-Guillarmod, F. Mulhauser, C. Piller, L.A. Schaller,
L. Schellenberg and H. Schneuwly

Institut de physique de l'Université, 1700-Fribourg, Switzerland

Abstract: Muonic hydrogen atoms transfer their muon in collisions to other elements. In transfer to neon, the yield of the resulting characteristic muonic X-rays can be used to determine the muon capture ratio in hydrogen to neon. The per atom capture ratio has been measured in three different gas mixtures H_2 + Ne at 15 bar, with neon concentrations of 0.7%, 1.4% and 2.0%. The per atom capture ratio A(H/Ne) has been found to be independent of the neon concentration with a value of about 1/16.

When negative muons are injected into matter, they are slowed down and finally captured by the Coulomb field of an atomic nucleus. Because the muonic atom is formed in an excited state, one can observe muonic X-rays of characteristic energies emitted by the μZ atom while deexciting to the ground state. The muonic hydrogen X-rays have very low energies (around 3 keV) such that in gaseous mixtures of hydrogen with rather small amounts of neon, only the muonic neon X-rays are easily detectable.

In H_2+Ne gas mixtures with small neon concentrations, one distinguishes two kinds of muonic neon X-rays, those which appear in coincidence with the incoming muon, called prompt events, and those which appear delayed. The last ones result from muons first captured in hydrogen and then transferred to neon from the μp_{1s} state. Their time structure corresponds to an exponential function with a time constant $\tau = 1/\lambda$, the lifetime of the μp_{1s} atoms in the given mixture (cf. Fig. 1).

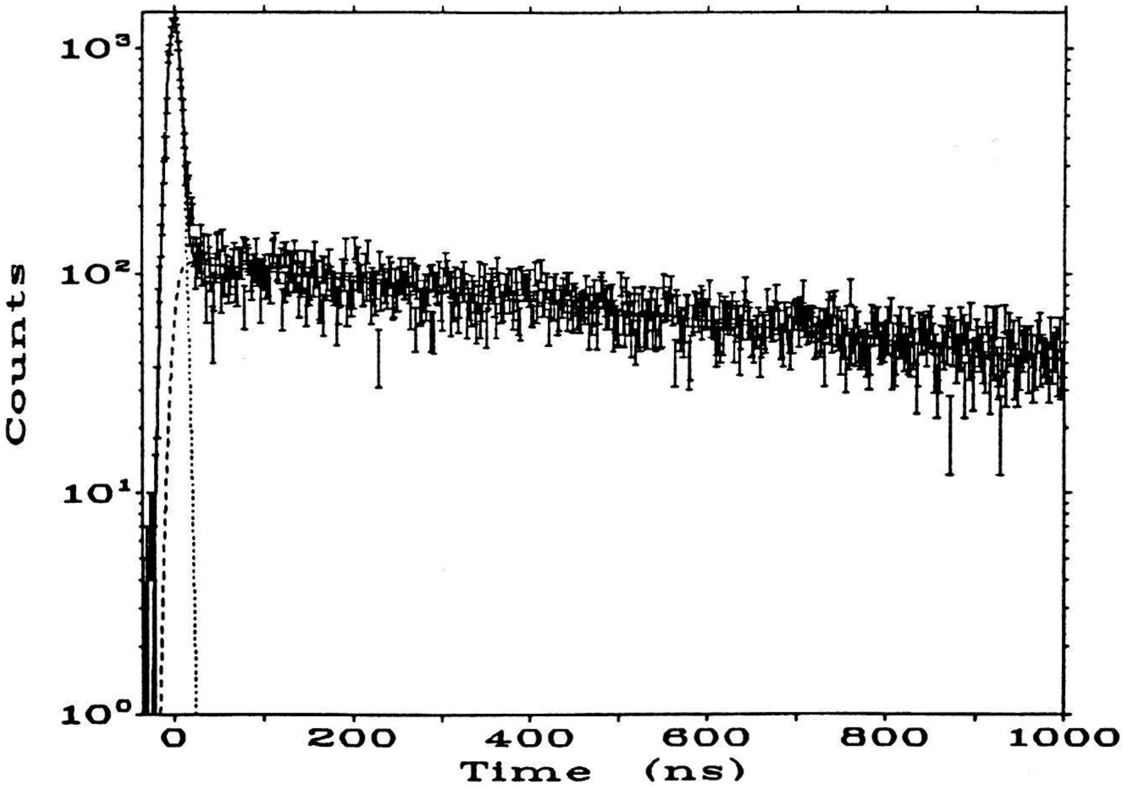

Figur 1: Time distribution of muonic neon μNe(2p-1s) X-rays measured in a H_2+0.7% Ne gas mixture. The prompt events correspond to the peak centered at t=0. The delayed events are due to muon transfer to neon from the μp_{1s} atom.

Actually, the μp atoms disappear not only by transferring their muon to neon, but also by muon decay with an associated rate λ_0, by formation of pμp molecules or by transferring the muon to deuterium or other impurities contained in the gaseous mixture. The total disappearance rate of the μp_{1s} atoms is then given by:

$$\lambda = \lambda_0 + \lambda_{p\mu p} + \lambda_{\mu d} + \lambda_{Ne} = 1/\tau$$

Since the rates λ_0, $\lambda_{p\mu p}$ and $\lambda_{\mu d}$ are known, the transfer rate to neon, λ_{Ne}, can be determined from the measurement of the total disappearance rate λ. To compare transfer rates to neon, measured in gaseous mixtures with different neon concentrations, it is usual to normalize them to the atomic density of liquid hydrogen, Λ_{Ne}.

Table 1 shows the mean lifetimes τ of μp_{1s} atoms measured in three H_2+Ne mixtures and the deduced normalized transfer rates, which agree reasonably well with each other. They disagree, however, rather strongly with preceding measurements[1, 2].

Table 1: Measured mean lifetimes, τ, of μp_{1s} atoms in three gaseous mixtures H_2+Ne at 15 bar and deduced normalized muon transfer rates Λ_{Ne}. The indicated uncertainties correspond to statistical errors only.

relative neon concentration [%]	τ [$. 10^{-9}$ s]	Λ_{Ne} [$\cdot 10^{11}$ s^{-1}]
0.7	936 ± 70	0.086 ± 0.006
1.4	640 ± 30	0.080 ± 0.004
2.0	499 ± 25	0.083 ± 0.004

If the assumption is made that the prompt muonic neon X-rays are due to direct muon capture, the relative yield of delayed to prompt events can be used to determine the muon capture ratio in hydrogen to neon [3]. The measured per-atom capture ratios, A(H/Ne), are given in Table 2. For all three investigated mixtures, the calculated per-atom capture ratios are the same, i.e. independent of the relative concentration which changes by a factor of three. They are, however, by a factor of two smaller than the corresponding pion capture ratio [4]. This difference points to a possible muon transfer from excited μp^* states to neon.

Table 2: Measured per-atom capture ratios A(H/Ne) in three gaseous H_2+Ne mixtures at 15 bar. The given uncertainties are statistical only.

relative neon concentration [%]	A(H/Ne)
0.7	0.0662 ± 0.0046
1.4	0.0653 ± 0.0032
2.0	0.0664 ± 0.0033

[1] A. Alberigi Quaranta, A. Bertin, G. Matone, F. Polmonari, A. Placci, P. Dalpiaz, G. Torelli and E. Zavattini, Nuovo Cimento B47, 92 (1967)

[2] R. Jacot-Guillarmod, F. Mulhauser, C. Piller and H. Schneuwly, Phys. Rev. Lett. 65, 709 (1991)

[3] H. Schneuwly, Nucl. Instrum. Methods B9, 97 (1985); 14, 258 (1986)

[4] V. I. Petrukhin and V. M. Suvorov, Zh. Eksp. Teor. Fiz. 70, 1145 (1976) [Sov. Phys.-JETP 43, 595 (1976)]

Principles of superheated superconducting granules as a detector for dark matter and neutrinos

C.Berger, G.Czapek, U.Diggelmann, M.Furlan, A.Gabutti, S.Janos, U.Moser, K.Pretzl, K.Schmiemann
Laboratory for High Energy Physics, University of Berne, Switzerland

Abstract: The interest in superconducting devices for particle detection is based on the very small quantum energies involved as compared to conventional ionization and semiconductor detectors. The use of superheated superconducting granules (SSG) as a particle detector is reviewed. Physical properties and experimental applications of SSG are discussed. The dynamic responses of the phase transition of superheated superconducting Sn, In, Al and Zn single granules (20-50μm in diameter) due to an applied magnetic field exceeding the superheating threshold are presented. A status report on further experimental development is given.

A SSG detector typically consists of tiny spherical granules (several μm in diameter) which are cooled down below their critical temperature T_c and are mounted in an applied magnetic field. The granules are made from type I superconductors, i.e. they have a superheating (H_{sh}) and supercooling (H_{sc}) phase transition. The grains serve as target and detector material at the same time. Interaction of an incoming particle within the target heats, due to thermal deposit of energy, one or several granules. In a uniform heating model the temperature change experienced by one granule is

$$\Delta T \approx \frac{3\,\Delta E}{4\pi\, c\, \rho\, R^3}$$

with ΔE the energy release of the particle in the grain, c the specific heat, ρ the density and R the radius of the grain. Since superheating happens in the presence of an applied magnetic field, the readout technique is based on the disappearance of the Meissner effect, where current loops placed around the granules detect a local variation in magnetic flux $\Delta\phi \sim \frac{H R^3}{D}$ (with D a loop dimension and H the applied magnetic field). The electronic signal is in general rather small, and detecting it may become a major challenge. If τ is the time the external magnetic flux needs to penetrate the grain (also called flipping time), the voltage pulse across the pickup loop is $\Delta V \sim \frac{\Delta\phi}{\tau}$.

From the above considerations the knowledge about the flipping time of our small granules is crucially important for the development of a SSG detector. The propagation of the magnetic field into the superconducting sphere is mainly conducted by the resistive damping of the induced eddy currents [1]. Evaluating the penetration process theoretically, the flipping time should follow the relation $\tau \sim \sigma R^2$, with σ the electrical conductivity of the normal material. Up to date there have been to our knowledge no experimental measurements with very small spheres. In our experiment the pickup coil and the amplifier were optimized such, that the bandwidth was large enough for the anticipated signal speed and that the signal-to-noise ratio was sufficient to detect flips of single granules of only 20μm diameter. Measurements of the transition time τ have been performed for Sn, In, Al and Zn, varying the grain size (20-50μm in diameter) , the orientation angle relative to the magnetic field and the bath temperature. Figure 1 shows a typical transition signal ($d\phi/dt$) and its integral ($\Delta\phi$) for a 40μm Sn grain at 2K (pulse is averaged over many magnetic field sweeps). The relation between flipping time and grain size $\tau \sim R^2$ could be clearly verified (Fig.2). By changing the

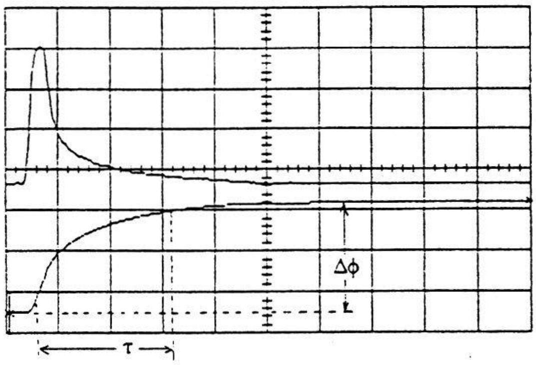

Fig. 1: phase transition pulse and integral of a Sn 40µm grain @ 2K (100ns,5mV/div)

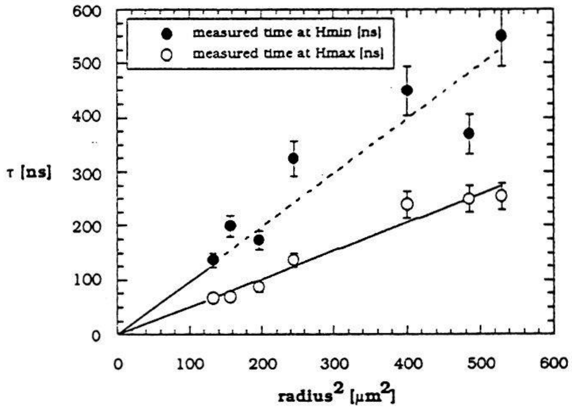

Fig.2: transition time $\tau \sim R^2$ of Sn grains (@ 1.5K) at the two orientations relative to the magnetic field

grain orientation in the field the superheating field H_{sh} shows a modulation of typically 16% [2] and τ varies by a factor of 2, which may be due to nucleation centers and the variation of the field penetration depth due to the crystal structure of the grain [3]. In addition we observed a dependence of the flipping time on the bath temperature (Fig.3). This can be consistently explained by the temperature and magnetic field dependence of the conductivity σ [4]. Furthermore a size effect on σ was observed (mean free path of the conducting electrons is in the range of the grain size). Table 1 lists the flipping time per R^2 at given operating temperature. The transition times are the same for magnetically and thermally induced transitions (global heating) within the experimental errors.

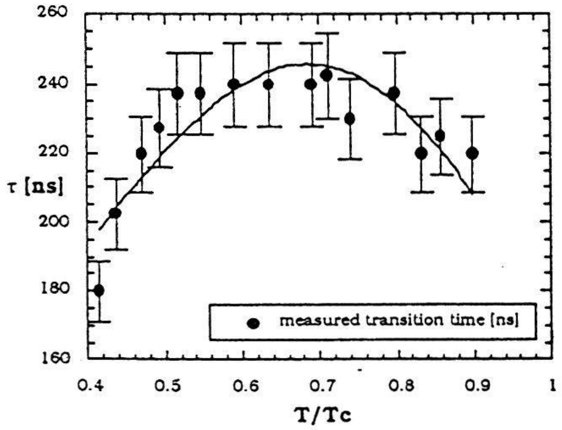

Fig.3: τ versus reduced temperature for 36µm Sn

material	Sn	In	Al	Zn
T [K]	1.8	1.7	0.48	0.47
$\frac{\tau}{R^2}\left[\frac{ns}{\mu m^2}\right]$	0.68	1.23	0.32	3.2

Tab.1: flipping time per surface for different materials

For a real SSG detector various readout systems can be implemented depending on the required spatial resolution and the number of channels that can be managed: from long hair-pin like loops forming x-y matrix and giving position information by time coincidence, to circular pad-like coils. Different types of low noise pre-amplifiers are also being developed. Much higher sensitivity can be reached by the use of SQUIDS if the experiments do not require very good time resolution.

We have tested SSG detector prototypes at the accelerator of PSI Switzerland in different particle beams in order to verify the expected efficiency. In the next future we're planning to perform an experiment with several grams of SSG detector mass in our underground laboratory.

Ref.: [1] A.B. Pippard, Phil. Mag. 41 (1950) 243
[2] M. Frank, P. Freund, J. Gebauer, K. Pretzl, A. Singsaas, L. Stodolsky, NIM A287 (1990) 583
[3] P.C.L. Tai et al., Phys. Rev., B11, 1 (1975) 411
[4] M. Furlan, diploma thesis, Univ. of Berne (1991)

Test of a Superheated Superconducting Granule Detector with nuclear recoil measurements

C. Berger [1], G. Czapek [1], U. Diggelmann [1], I. Flammer [1], D. Frei [1], M. Furlan [1], A. Gabutti [1], S. Janos [1], U. Moser [1], K. Pretzl [1], K. Schmiemann [1], D. Perret-Gallix [2], B. van den Brandt [3], J.A. Konter [3], S. Mango [3].
1) Laboratory for High Energy Physics, University of Bern, CH-3012 Bern, Switzerland
2) LAPP Annecy, France
3) Paul Scherrer Institute, CH-5232 Villigen PSI, Switzerland

The presented results are part of a Superheated Superconducting Granule (SSG) detector development for neutrinos and dark matter. An aluminum SSG detector was exposed to a 70MeV neutron beam to test the detector sensitivity to nuclear recoils. The neutron scattering angles were determined using a scintillator hodoscope. Coincidences between the SSG and the hodoscope signals have been clearly established. Data were taken at an operating temperature of 120mK for different SSG intrinsic thresholds. The proved sensitivity of the detector to nuclear recoils above 10keV is encouraging for possible applications of SSG as a dark matter detector.

Superheated Superconducting Granule (SSG) devices are being presently developed for the detection of neutrinos and dark matter candidates. The proposed detection principle for neutrinos and weakly interacting massive particles (WIMPs) is based on neutral current interactions [1] (coherent scattering) with a nucleus inside the granule. A recent review of the status of the SSG detector development can be found in Ref. [2].

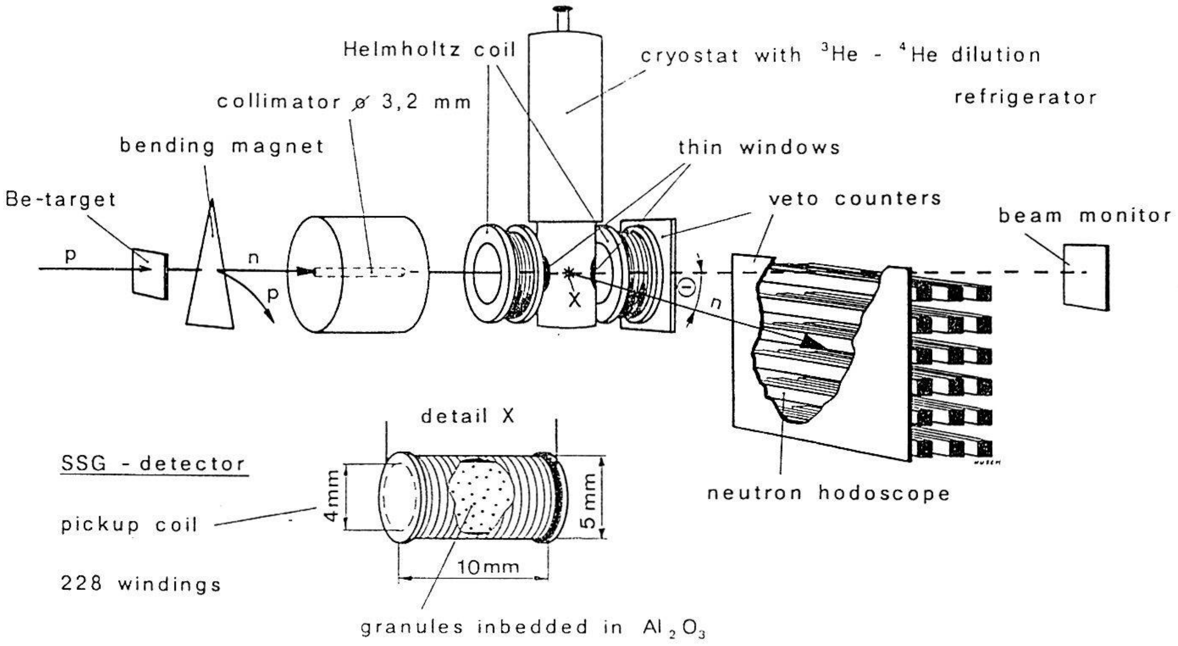

Fig. 1 Experimental setup.

To study the detector sensitivity to nuclear recoils, an aluminum SSG device has been irradiated with a 70MeV neutron beam at the Paul Scherrer Institute (Villigen-Switzerland). The setup used in our experiment is sketched in Fig. 1. The SSG detector consisted of a hollow Teflon cylinder of 4mm inner diameter and 8mm inner length, filled with about 780 000 aluminum granules of diameter between $20\mu m$ and $25\mu m$. The granules were embedded in a dielectric matrix made of an Al_2O_3 granulate with a 6% volume filling factor. To sense the phase transition of the exposed granules, the SSG target was surrounded by a pickup coil with 228 windings connected to a J-FET preamplifier working at room temperature. The detector was operated at a constant temperature of 120mK±10mK. To detect the scattered neutrons, a scintillator hodoscope, consisting of 18 scintillator elements arranged in three parallel planes perpendicular to the beam direction, was placed 2 meters downstream of the SSG detector [3].

The scattering angles were determined from the position of the interacting particle inside a single element and the covered range of scattering angles was 0.02-0.5rad±20mrad. To discriminate against charged particles leaving the SSG, two veto counters were installed between the cryostat and the hodoscope. The irradiation experiment consisted of many consecutive cycles. In each cycle the applied magnetic field was raised to the reference value H_1=104Gauss, lowered at the value H_2 and maintained constant for 5 minutes. The beam induced phase transitions were recorded only during the plateau time. At the end of the cycle, the detector was reset lowering the applied magnetic field to zero. Data were taken at three different detector thresholds $\Delta H/H=(H_1-H_2)/H_1$ of 2%, 5% and 10%. Neutron induced events were selected with opportune off-line selection cuts from the coincidences between the radio frequency of the beam injector, the SSG and the hodoscope counters (see Ref. 3 for details). In the data analysis, only events from the selected sample with no signal from the veto counters were considered to reduce the contamination due to charge exchange reactions within the SSG, which yielded a fast proton in the final state. After those cuts we were left with about 300 events for each detector threshold.

$\Delta H/H$ [%]	E_r (exp) [keV]	E_r (MC) [keV]
2	30±5	30±5
5	45±7	40±8
10	65±10	70±10

Table 1. Experimental (exp) and calculated (M.C.) values for the recoil energies E_r in the threshold region at half maximum

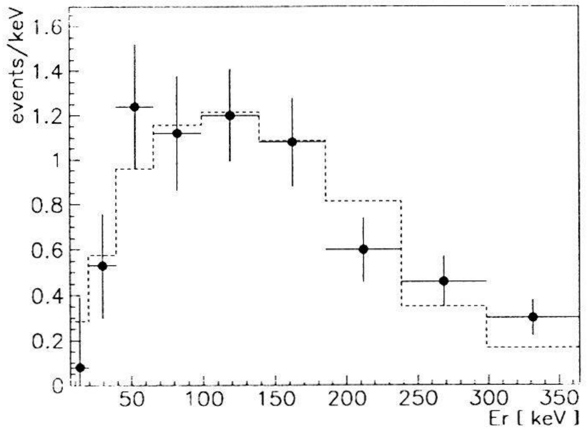

Fig. 2 Recoil energy distributions derived by Monte Carlo (histogram) and measurements (points) for a detector threshold ΔH/H=2%.

To investigate the detector sensitivity to nuclear recoils, the measured recoil energy distributions were compared to Monte Carlo simulations. From the phase diagram and the measured distribution of superheating fields, the calculated recoil energies were related to the detector thresholds ΔH/H [3]. The comparison between the calculated and measured values of the recoil energies are reported in Table 1. The experimental errors are due to the spatial resolution of the hodoscope, the statistical and the systematical errors of the selection cuts.

The calculated values have an error due to the theoretical uncertainty of the partial wave expansion. The calculated and measured recoil energy distributions for a detector threshold ΔH/H=2% are shown in Fig. 2. The measurements follow the theoretical predictions confirming that aluminum granules (23 μm in diameter) can be successfully used to detect recoil energies around 10keV. The results indicate that the detector response to recoil energies allows in principle, to reach much smaller energy thresholds (in the electron volt region) with granules of smaller diameters. We are planning in the near future to extend these measurements to smaller recoil energies using other granule materials like Zn and Sn. For a SSG dark matter detector it is planned to use more sensitive SQUID-loops readout (Superconducting Interference Device) to have larger detector volumes.

References [1] M.W Goodman and E. Witten, Phys. Rev. D 12 (1985) 3059.
[3] C. Berger et al, to be published in NIM A.
[2] K. Pretzl, Particle World Vol. 1, N.6 (1990) 153.

Remote Imaging of Ion Distributions Using Low Energy Neutral Atoms

Peter Wurz[1], Peter Bochsler[1], Arthur G. Ghielmetti[2], Edward G. Shelley[2], Federico Herrero[3] and Mark F. Smith[3]

[1]) Physikalisches Institut, Universität Bern, Sidlerstrasse 5, 3012 Bern, Switzerland
[2]) Lockheed Palo Alto Research Laboratory, Dept. 91-20, 3251 Hanover Street, Palo Alto, CA 94304, U.S.A.
[3]) Laboratory for Extraterrestrial Physics, NASA/Goddard Space Flight Center, Greenbelt, MD 20771, U.S.A.

The scope of the neutral atom imaging instrument on the proposed HI-LITE mission is to study the instantaneous global distribution of the low energy ion outflow from the high latitude auroral region, and its large scale temporal evolution with solar and geomagnetic activity by detecting neutral atoms, produced through charge exchange between the out flowing ions and the neutral atmosphere. The proposed instrument will record maps of energy and mass flux of the source region. For satisfactory performance, high ionization efficiency for the two species of principal interest, H and O, in the energy range of 10 eV to 300 eV is required. To achieve this, surface ionization will be employed, where a considerable fraction of the reflected primary atoms will be negatively ionized.

One of the major objectives of space physics is to understand the Earth's magnetosphere and its interaction with the ionosphere and the solar wind, which is important in the high-latitude regions of the Earth's magnetosphere. Input from the solar wind produces significant effects on the Earth's ionosphere including auroral displays and upwelling of ionospheric ions that ultimately become part of the magnetospheric population, and interact back on the ionospheric plasma. If the amount of solar wind mass, energy, and momentum added to the magnetosphere is high, the system becomes highly disturbed and the imparted energy is dissipated explosively through the substorm process. Geomagnetic activity also plays an important role for the ion outflow in these regions [1,2]. To enhance the understanding of these highly variable processes, the demands on the HI-LITE mission [3] are both global observation of the entire source region, and a time resolution commensurate with the time scale of these mechanisms.

The proposed instrument will record spatially resolved maps of energy and mass of this region. Most of the parts of the proposed instrument for this mission are state-of-the-art in space science instrumentation, the only new technology is the surface ionization. Fig. 1 shows a cross section of the instrument schematics [4]. The instrument consists of an entrance collimator, a conversion unit, a pre-acceleration lens, an electrostatic analyzer, and a time-of-flight (TOF) mass analyzer with position sensitive detection. The rotational symmetry of the instrument about the centerline of the figure gives a 90° field-of-view in the plane normal to the figure

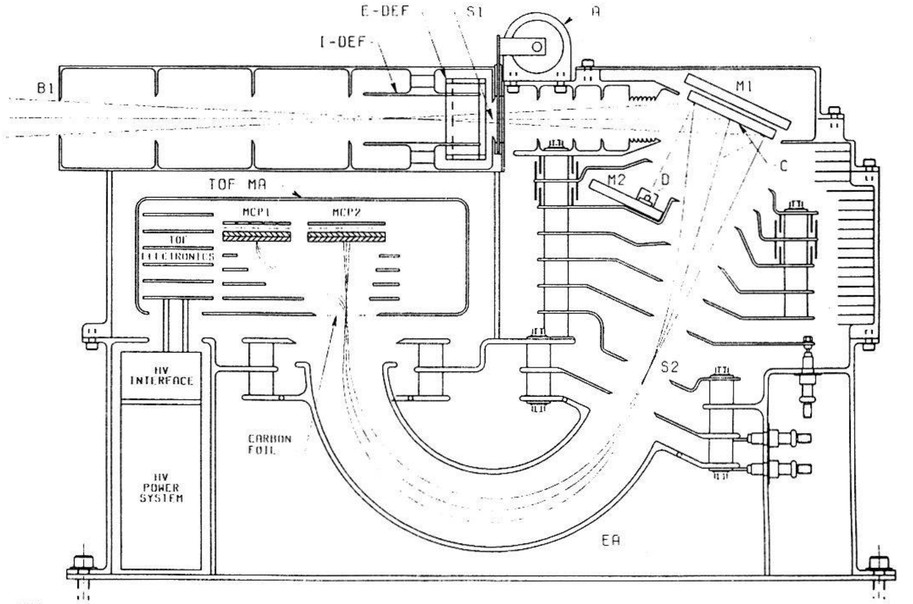

Figure 1: Schematic instrument drawing: with entrance collimator B1, ion and electron deflectors I-DEF and E-DEF, shutter S1, converter surface C, secondary electron suppression magnets M1 and M2, cesium dispenser D, energy limiting slit S2, and EA and MA are the energy and mass analyzers.

with imaging over the entire range of accepted angles. The required high sensitivity is achieved with a large geometric factor and with simultaneous imaging in angle, energy, and mass parameter space, which by eliminating the scan in angle, mass, and energy increases the time resolution significantly. Double coincidence detection in the TOF analyzer coupled with high UV rejection insure the low background countrates needed.

Since the efficient ionization of neutral particles is the crucial part of this instrument it will be covered in more detail here. Particles are reflected from a surface as negative ions if they have a positive electron affinity and the work function of the surface is sufficiently low [5]. For hydrogen and oxygen the electron affinities are 0.75 eV and 1.46 eV. The surface with the lowest work function is W(110) covered with half a monolayer of cesium. For the overall detection efficiency, the probability for particle reflection from the surface has to be convoluted with the fraction of particles reflected as negative ions [6]. Two configurations were investigated: a polycrystalline tungsten substrate covered either with half a monolayer or a full monolayer of Cs for hydrogen impacting at angles from 0° to 85° and of 10 to 300 eV energy. Due to the higher electron affinity for oxygen, a higher detection efficiency is anticipated. As can be seen from Fig. 2, for half a monolayer Cs coverage the detection efficiency is about a factor of 5 higher than for full Cs coverage. Therefore, in the instrument we intend to use half a monolayer Cs on a W(110) surface. At an impact angle of 65° the detection efficiency will be between 11% and 25% for hydrogen in the energy range from 10 to 300 eV. Making the impact shallower would increase the detection efficiency somewhat, but also increase the surface area that has to be maintained in proper condition. Moreover, the design of the ion optical system would be more difficult and ultimately would increase weight. Currently, we are carrying out a detailed feasibility study for the applicability of surface ionization to space instrumentation.

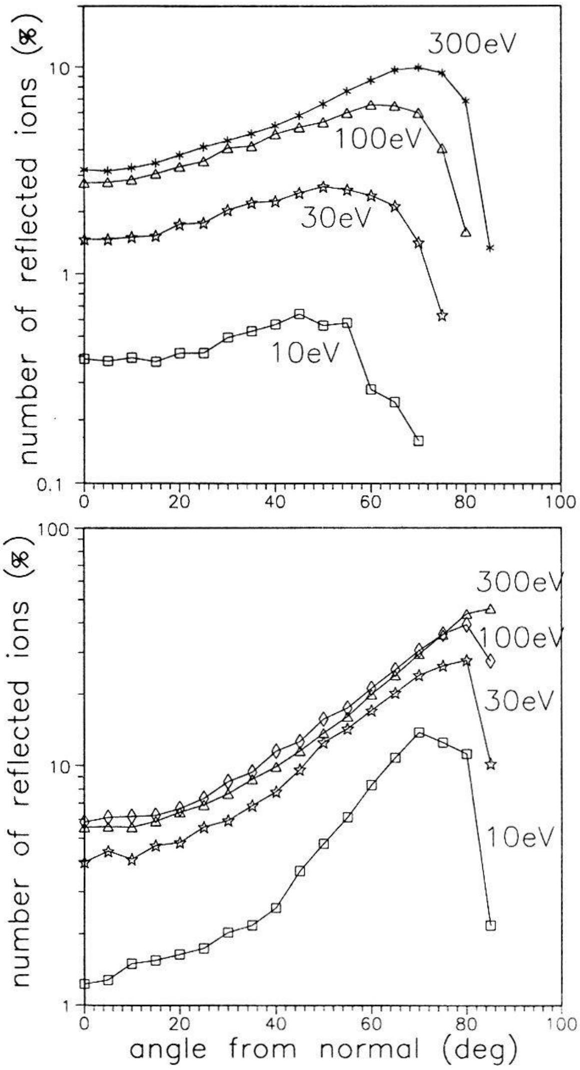

Figure 2: Convolution of the ionization probability with the reflection probability for hydrogen atoms of 10, 30, 100 and 300 eV impinging on a tungsten surface covered with 1 and 0.5 monolayer of cesium, (top panel and bottom panel).

The financial support by the *Swiss National Science Foundation* is gratefully acknowledged.

[1] D.T. Young, H. Balsiger, J. Geiss, J. Geophys. Res., **87**, 9077 (1982).

[2] A.W. Yau, E.G. Shelley, W.K. Peterson, and L. Lenchyshyn, J. Geophys. Res., **90**, 8417 (1985).

[3] A detailed mission description is given in: M.F. Smith, et al., SPIE proceedings, submitted (1993).

[4] A detailed instrument description is given in: A.G. Ghielmetti, E.G. Shelley, F. Herrero, M.F. Smith, P. Wurz, P. Bochsler, and T. Stephen, SPIE proceedings, submitted (1993).

[5] J. Los, and J.J.C. Geerlings, Phys. Reports, **190**, 133 (1990).

[6] C.F.A. van Os, and P.W. Amersfoort, J. Los, J. Appl. Phys. **64**, 3863 (1988).

Quantum Phase Space of Two-Spin Systems

N. Regez, W. Breymann, H. Thomas
Institut für Theoretische Physik, Universität Basel, CH-4056 Basel

We present results of numerical experiments performed on quantum two-spin systems, which permit a direct comparison of quantum and classical invariant structures. Two complementary representations are discussed: Husimi distributions, i. e., the decomposition of stationary states in terms of coherent states, and a second type of distribution which gives a measure of localization of coherent states during time evolution.

We have investigated the quantum phase space for a class of two-spin systems given by the following Hamiltonian:

$$H = -J\left\{(1+\gamma)\,S_{1x}S_{2x} + (1-\gamma)\,S_{1y}S_{2y} + \frac{\alpha}{2}\left(S_{1x}^2 - S_{1y}^2 + S_{2x}^2 - S_{2y}^2\right)\right\}.$$

The model parameters γ and α describe the anisotropy of the exchange interaction and the crystal-field energy, respectively, and J represents the exchange integral. The motion of the corresponding classical systems in four-dimensional phase space has been investigated for various values of α and γ in [1].

For a comparison of classical phase-space structures with quantum properties one needs two features:

1. A mapping from classical phase space Γ onto quantum Hilbert space **H**. For that purpose we have used coherent two-spin states $|\Omega\rangle$, which are parametrized by the classical phase space variables.

2. Invariant functions on Hilbert space **H**: Any function of the N projection probabilities $|c_n|^2 = |\langle E_n|\Omega\rangle|^2$ of the state $|\Omega\rangle$ onto the eigenstates $|E_n\rangle$ of the Hamiltonian satisfies the requirement to be invariant under the motion ($N = \dim \mathbf{H}$).

The function $W_n = |\langle E_n|\Omega\rangle|^2$ for a fixed eigenstate $|E_n\rangle$ is called the Husimi distribution of that state. It represents the decomposition of the state $|E_n\rangle$ in terms of coherent states. We have calculated Husimi distributions and compared them with classical phase-space structures. The function W_n is localized along some classical orbit with energy $E_{cl} \approx E_n$. The patterns formed by the zeros of W_n have also been studied: Their deviation from a linear distribution is a measure for the non-integrability of the corresponding classical system, confirming results from [2].

A second type of invariant functions is given by

$$\mathcal{N}_\infty^{-1} = \sum_n |\langle E_n|\Omega\rangle|^4$$

for non-degenerate Hamilonians [3]. $\mathcal{N}_\infty^{-1}$ is a measure for the inverse number of phase space cells of volume h^2 explored by the state $|\Omega\rangle$ during time evolution, and therefore a measure for its localization. We have calculated the scaling of $\mathcal{N}_\infty^{-1}$ with spin length s. By considering the minimum uncertainty of the state $|\Omega\rangle$ and the dimension of the invariant sets in classical phase space, one expects the following scaling behavior, depending on the type of orbit on which the classical phase point corresponding to $|\Omega\rangle$ lies: $\mathcal{N}_\infty^{-1} \propto s^{-1/2}$ for periodic orbits, $\mathcal{N}_\infty^{-1} \propto s^{-1}$ for quasiperiodic orbits, and $\mathcal{N}_\infty^{-1} \propto s^{-3/2}$ for chaotic orbits.

The scaling of $\mathcal{N}_\infty^{-1}$ with spin length s has been calculated for three different systems. The coherent states considered satisfy the Poincaré surface-of-section conditions: $\vartheta_2 = \frac{\pi}{2}$, $\dot{\vartheta}_2 > 0$ and $\langle\Omega|H|\Omega\rangle = E_{cl}$, corresponding to the conditions chosen for the investigation of the classical systems in [1]. The results shown are for $\vartheta_1 = \frac{\pi}{2}$, $\varphi_1 \in [0, 2\pi]$.

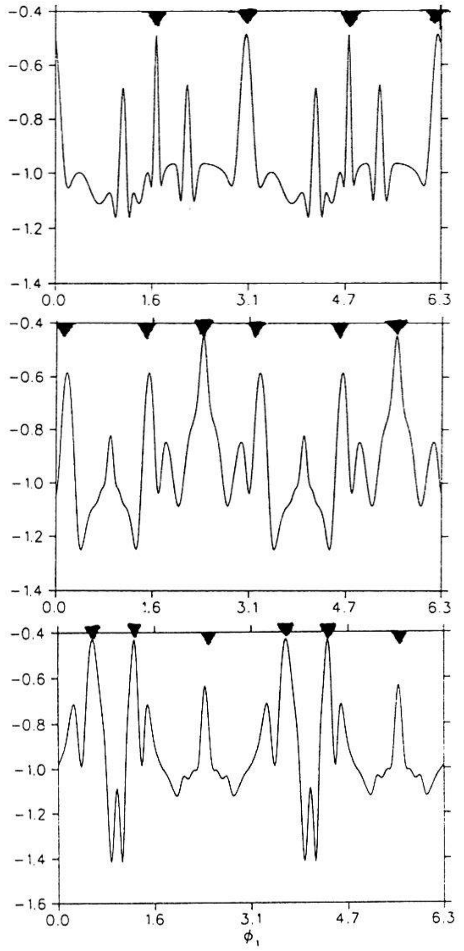

(a) $\alpha = 0$, $\gamma = 0.5$ (classical system fully integrable): The shortest stable periodic orbits are represented by a scaling exponent of 0.5 (arrows). Unstable periodic orbits have an exponent of about -0.7. In between, $\mathcal{N}_\infty^{-1}$ scales with an exponent of about -1.0 for all states, the value expected for quasiperiodic orbits.

(b) $\alpha = 0.5$, $\gamma = 0$ (classical system weakly non-integrable): The maximum values of -0.45 of the scaling exponent correspond to stable periodic orbits (arrows). The other peak values indicate either stable (arrows) or unstable (no arrows) periodic orbits. The fact that nowhere a value below -1.25 is assumed can be explained by the fact that the chaotic regions are very narrow.

(c) $\alpha = 0.7, \gamma = 0$ (classical system strongly non-integrable): The peaks correspond to periodic orbits, the stable ones being marked by arrows. The smallest scaling exponents occur within the chaotic sea, the low values of around -1.4 reflecting its large extension.

The maxima of the scaling exponents correspond to periodic orbits for the three systems considered. Furthermore, the values of the scaling exponent agree rather well with our expectations.

The numerical calculations have been performed on SX-3 at the CSCS in Manno (TI). The attribution of computation time is greatly acknowledged.

[1] N. Srivastava, C. Kaufman, G. Müller, R. Weber, H. Thomas. *Integrable and Nonintegrable Classical Spin Clusters.* Zeitschr. f. Phys. B**70**, 251 (1988)

[2] P. Leboef, A. Voros. *Chaos-Revealing Multiplicative Representation of Quantum Eigenstates.* J. Phys. A**23**, 1765 (1990)

[3] E. J. Heller. *Quantum Localisation and the Rate of Exploration of Phase Space.* Phys. Rev. A**35**, 1360 (1986)

Marginal Dependence of the Ba Site Dipole - Field from Cu *d* - Electron Anisotropies in Antiferromagnetic $YBa_2Cu_3O_6$

E.P. Stoll

Physik-Institut, Universität Zürich - Irchel, Winterthurerstr. 190, CH - 8057 Zürich

To determine the local magnetic field which can be measured with NQR on a barium site in antiferromagnetic $YBa_2Cu_3O_6$ the dipole field is computed by evaluating the integrals over the spherical functions of delocalized magnetic *d* - electrons. The results of these calculations show that the effect of finite size and anisotropy of the Cu 3*d* electrons is only in the order of a few percents.

Recently [1], NQR measurements in antiferromagnetic (AF) $YBa_2Cu_3O_6$ ($T_N = 418K$) at $T = 82K$ have shown the existence of a magnetic field of 148 Gauss perpendicular to the *c*-axis at the Ba sites. Calculations of the dipole field by assuming localized moments of 0.64 μ_B lying in the Cu-O plane at the antiferromagnetically ordered Cu sites gave a much larger field of $\sim$ 470 Gauss. To explain such a deviation, the dipole field is recomputed by evaluating the contributions from the delocalized wave functions of the magnetic *d* - electrons.

According to [2], the dipole field at $\mathbf{R}$ is given by

$$B_i(\mathbf{R}) = \sum_{\mathbf{m}} D_{i,j}(\mathbf{m} - \mathbf{R})\mu_j(\mathbf{m}) \tag{1}$$

with magnetic moments μ_j localized at lattice sites $\mathbf{m}$.

To take into account the anisotropy and the finite size of the Cu *d* - shells, the functions D_{ij} and μ_j have to be integrated over the whole space:

$$\overline{B_i}(\mathbf{R}) = \sum_{\mathbf{m}} \int d^3\mathbf{r} D_{i,j}(\mathbf{r} - \mathbf{R})\mu_j(\mathbf{m} - \mathbf{r}). \tag{2}$$

Furthermore [2], the operator D_{ij} is given as

$$D_{ij}(\mathbf{x}) = (\nabla_i\nabla_j - \frac{1}{3}\delta_{ij}\Delta)\frac{1}{x} - \frac{2}{3}\delta_{ij}\Delta\frac{1}{x}. \tag{3}$$

Because the difference ($\mathbf{m}$ - $\mathbf{r}$) remains fixed during the derivation with respect to $\mathbf{R}$, the $\Delta(1/x)$ - function in (3) vanishes.

The electron wave functions ψ and therefore also the electron densities $\rho=|\psi|^2$ of the magnetic atoms can be expanded in spherical Y_{lm} and radial R_{nl} functions

$$\psi_{nlm} = R_{nl}(r)Y_{lm}(\theta, \phi) \tag{4}$$

and

$$\rho = R_{nl}^2(r)\sum_{j=0}^{l} a_{jlm}Y_{2j,0}(\theta,\phi). \tag{5}$$

The function $1/x=1/(|\mathbf{r}-\mathbf{R}|)$ in (3) also can be expanded in terms of $Y_{l'm'}(\theta',\phi')$.

$$\frac{1}{|\mathbf{r}-\mathbf{R}|} = 4\pi\sum_{l=0}^{\infty}\sum_{m=-l}^{l}\frac{1}{2l+1}\frac{A^l}{B^{l+1}}Y_{lm}^*(\theta',\phi')Y_{lm}(\theta,\phi), \tag{6}$$

with $A = |\mathbf{m}-\mathbf{r}|$ and $B = |\mathbf{m}-\mathbf{R}|$, if $|\mathbf{m}-\mathbf{r}| < |\mathbf{m}-\mathbf{R}|$, and $A = |\mathbf{m}-\mathbf{R}|$ and $B = |\mathbf{m}-\mathbf{r}|$, elsewhere.

Due to the fact that the spherical functions Y_{lm} are orthonormal, and by exchanging derivation (3) and integration over the solid angle, the dipole field $\overline{B_y}$ (2) can be calculated from the knowledge of the a_{jlm} in eq. (5).

To estimate the influence of delocalized wave functions on the value of the induced dipole field, the radial function $R_{3,2}(r)$ of the Cu $3d$ - electrons was taken from self - consistent free atom calculations according Ref.[3].

	$\overline{B_y}/B_y$		
m	$(\theta=0)\Vert x$	$(\theta=0)\Vert y$	$(\theta=0)\Vert z$
0	0.96602	0.96602	1.03399
1	0.99614	0.99614	1.02992
2	1.02063	1.02063	0.95285

Table 1: Relation between extended and localized Cu d - shell calculations of the dipole field at a Ba atom for different magnetic quantum numbers m. The values have been obtained from summing over 16 AF Cu atoms in the next neighbor planes and 4 atoms in the next-next neighbor planes with magnetic moments parallel the x - direction.

As it is shown in Table 1, the dipole field $\overline{B_y}$ in the y - direction according (2) deviates only a few percents from B_y (1). Therefore, the deviation between NQR measurements and calculations can not be explained by the Cu d -shell anisotropy.

P. Blöchl, M. Mali, P.F. Meier and J. Roos are acknowledged for valuable discussions.

References

[1] M. Mali and J. Roos (1993) (unpublished).

[2] P.F. Meier, W. Kündig, B.D. Patterson, and K. Rüegg, Hyperfine Interactions **5**, 311 (1978).

[3] J.P. Perdew and A. Zunger, Phys. Rev. B**23**, 5048 (1981).

LE SPECTRE DE LA PHYLLOTAXIE

J. GUERREIRO et M. KUNZ
Institut de Physique Expérimentale, Université de Lausanne

The usual dynamical approach to phyllotaxis is presented. Distinction between rational and irrational numbers is shown to be a generic feature of these models, related to a convexity/concavity property.

L'apparition systématique du nombre d'or, jointe à l'absence de nombres rationnels, dans les structures spiralées qui se forment lors de la croissance d'une plante a depuis longtemps éveillé la curiosité des scientifiques.

Toutes les approches dynamiques de la phyllotaxie (littéralement "arrangement des feuilles") proposées jusqu'ici se ramènent à l'étude d'une classe de systèmes dynamiques à temps discret dont voici un prototype simple: soit f une fonction périodique sur $\mathbb{R}$ de période 1, symétrique autour de 0, continue et décroissante entre 0 et 1/2. Soit encore:

$$X = (x_1,\ldots,x_n) \in [0,1[^n$$

et associons à ce vecteur la fonction:

$$F_{X,\lambda}(s) =: \lambda^n f(s) + \sum_{i=1}^{n} \lambda^{n-i} f\Big(s - \sum_{k=1}^{i} x_k\Big), \quad n \in \mathbb{N}, \quad \lambda \in [0,1].$$

Définissons $g(X) \in [0,1[$ de telle manière que le point

$$\sum_{k=1}^{n} x_k + g(X)$$

soit l'abcisse du minimum absolu de $F_{X,\lambda}$. Si $F_{X,\lambda}$ possède plusieurs minima absolus dans $[0,1[$, on choisira celui qui est le plus proche de 0.
On définit alors l'application suivante:

$$\begin{aligned} G_{f,\lambda}:\ & [0,1[^n \to [0,1[^n \\ & X = (x_1,..,x_n) \mapsto G_{f,\lambda}(X) = (x_2,..,x_n,g(X)) \end{aligned}$$

L'itération de cette application définit un système dynamique dont les points fixes sont des vecteurs homogènes:

$$X_\theta = (\theta,\ldots,\theta).$$

Le nombre θ correspond précisément, dans ces modèles, au paramètre des structures botaniques envisagées dont la valeur observée approche le nombre d'or ou le nombre de Lucas. Il s'agit de savoir si notre modèle opère cette même sélection. Considérons le cas où f est convexe sur $\mathbb{R}\setminus\mathbb{Z}$. Pour un tel f, et n = 31, la figure 1 montre le spectre $\theta(\lambda)$ obtenu en itérant $G_{f,\lambda}$ à partir d'une certaine condition initiale X_0. Avec ce choix, on découvre un plateau autour du nombre d'or (= 0.382...) et un autre autour du nombre de Lucas (= 0.276...).

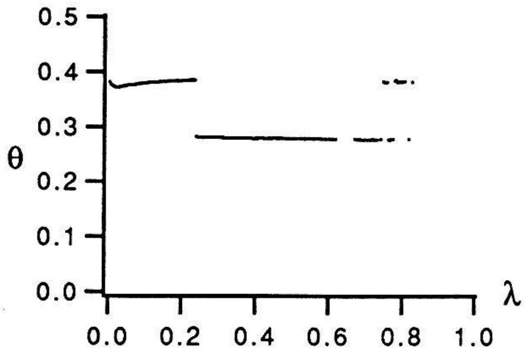

Fig. 1

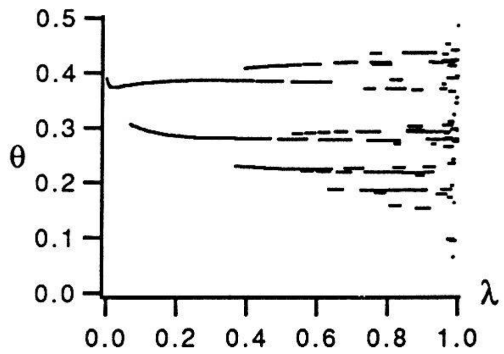

Fig. 2

Appelons A le spectre qu'on obtient en considérant toutes les conditions initiales possibles. C'est l'ensemble des points fixes de $G_{f,\lambda}$, que l'on peut définir explicitement de la manière suivante:

$$A = \{(\lambda,\theta) \in [0,1]\times[0,1/2] : (n+1)\theta \text{ est un minimum absolu de } F_{(\theta,\ldots,\theta),\lambda}\}$$

Nous voyons que A, illustré dans la fig. 2 pour les mêmes f et n que dans la fig. 1, présente une structure beaucoup plus riche. En particulier, le spectre A comporte toujours des branches non réduites à un point qui coupent l'axe $\lambda = 1$ sur toutes les valeurs rationnelles du type $\theta = p/(n+1)$, avec pgdc(p,n+1) = 1. La complexité de A croît ainsi avec n.

Dans le cas $n = \infty$, le spectre A présente des propriétés remarquables: c'est un ensemble dont tous les points sont d'ordonnée irrationnelle, et dont aucun point d'ordonnée rationnelle n'est point d'accumulation.

Il est crucial de remarquer que cette distinction des nombres en fonction de leur caractère irrationel - il s'agit là d'une des caractéristiques génériques essentielles de ces spectres - dépend du caractère convexe de f. En fait, si f est concave sur $\mathbb{R}\setminus(\mathbb{Z}+1/2)$, le spectre A jouit de propriétés équivalentes si l'on remplace le mot minimum par le mot maximum dans sa définition. Il existe ainsi une parfaite dualité de la théorie.

Cette dualité subsiste lorsque l'on considère n fini et f différentiable, soit convexe sur $[\varepsilon, 1-\varepsilon]$ soit concave sur $[-1/2+\varepsilon, 1/2-\varepsilon]$. Dans le premier cas, si $|\theta - p/q| > \varepsilon/q$, $\forall\, p,q \in \mathbb{N}$ et $1 \leq q \leq n$, il suffit que $(n+1)\theta$ soit un point stationnaire de $F_{(\theta,\ldots,\theta),\lambda}$ pour que ce soit aussi un minimum relatif. Dans le second cas, inversément, pour que $(n+1)\theta$ soit un minimum relatif de $F_{(\theta,\ldots,\theta),\lambda}$, il faut qu'il existe $p,q \in \mathbb{N}$, q pair et $1 \leq q \leq 2n$, tels que $|\theta - p/q| < \varepsilon/q$.

Il est important de noter que ces résultats sont valables pour une classe de systèmes beaucoup plus large que celle qui est présentée ici.

Nous tenons à remercier F. Rothen, A.-J. Koch, A. Joyet et G. Bernasconi.

Quelques références :

J. H. M. Thornley, Ann. Bot. 39, **491** (1975)
C. Marzec, J. Kapraff, J. Theor. Biol. **103**, 201 (1983)
J. Guerreiro, Thèse de Doctorat, à paraître